

Thesis

(draft)

Attila Dobi

Aug-13-2014

Contents

1 Calibrating the Combined Energy Scale	3
1.1 Anti-Correlation Space	4
1.2 Refitting in Combined Energy Space	6
1.3 Finding Errors with MCMC	8
1.4 Combined Energy Space	11
1.5 Light Collection and Electron extraction	12
2 Modeling Intrinsic Detector Resolution	12
3 Measuring Recombination Fluctuations	15
3.1 Measuring Recombination Fluctuations with Mono-Energetic Sources	15
3.2 Results with Mono Energetic Calibration Sources	17
3.3 Measuring Recombination Fluctuations in Desecrate Energy Bins	19
3.4 Measuring the Fano Factor in Bins of Energy	22
3.5 Application to ^{83}Kr	22
3.6 Application to Tritium Data (any continuos spectrum)	24
3.7 Centriod Subtraction	26
4 Correcting the Tritium Spectral Shape for Finite Resolution	28
4.1 Calculating the Observed Energy	29
4.2 Smearing a Toy Spectrum	31
5 Measuring LQ, QY and Recombination, Uncorrected for Spectral shape	33
5.1 Tritium S1 Mean and NEST	33
5.2 Tritium S2 Mean and NEST	33
5.3 Tritium Energy Spectrum	35
5.4 LY, QY, σR Result	36
6 The Standard Candle. Light Yield from $^{83\text{m}}\text{Kr}$	37
6.1 Field dependence of light yield from the 32.1 keV gamma of $^{83\text{m}}\text{Kr}$	38
7 Scintillation Yield and Ionization Yield from Tritium Beta Decay	39
7.1 Cuts used in this analysis	39
7.2 Results at 180 [V/cm], Corrected for Spectral Shape	40
7.3 Results at 100 [V/cm], Corrected for Spectral Shape	40
7.4 Compared With recent Compton Scattering Measurement	40

8	Fixing the Low Energy Tritium ‘Pile Up’	42
9	Discrimination vs E and S1	44
9.1	Discrimination vs. S1	44
9.2	Discrimination vs. Combined Energy	44

1 Calibrating the Combined Energy Scale

This section outlines the method used to calibrate the energy scale of the dual phase LUX detector. The ideal behind the method is to take calibration data with multiple sources and/or electric fields and combine the measured scintillation signals, primary (S1) and secondary (S2) in order to reconstruct energy. For a given energy deposit in liquid xenon an amount of quanta released is proportional to a work function W , for nuclear recoils we must also consider heat loss. The quanta created at the interaction site are the results of electron-ion pairs and exitons produced by the recoiling xenon nucleus, equation 1. Exitons quickly de-excite and contribute to the primary scintillation signal (S1). Ions that recombine with their electron pairs produce scintillation light (S1), while those electrons that do not recombine are collected several μs later in the extraction region as the larger secondary scintillation signal S2. We have two knobs to turn to probe combined energy space over a variety of S1 and S2, we can either change the energy of the source or adjust the drift field. The larger the spread in S1 and S2 the more constrained the combined energy scale will be. Measuring both light and charge allows for a vastly improved resolution compared with only using a single S1 or S2 only space, since recombination fluctuations cancel out if energy is reconstructed correctly.

$$\begin{aligned} E &= W \times n_q + \text{Heat} \\ E &= W(n_i + n_{ex}) + \text{Heat} \\ E &= W(n_\gamma + n_e) + \text{Heat} \end{aligned} \tag{1}$$

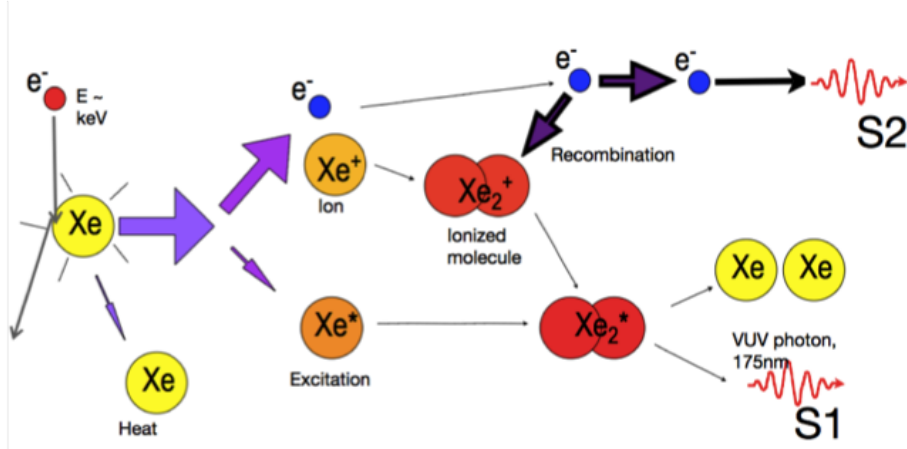


Figure 1: Diagram of an electronic recoil in liquid xenon.

Using equation 1 and assuming that the heat loss is negligible for electronic recoils (ER) above 1 keV we can reconstruct energy by knowing the work function and the conversion from measured S1(light) and S2(charge) signals to the number of quanta ($n_\gamma + n_e$) liberated by

the interaction. We define gain-1 (g_1) and gain-2 (g_2) as the conversion from initial number of photons and electrons propagated from the interaction site to the observed signal by the PMT arrays as a photo electron (PE), given in equation 2. By using multiple mono energetic sources with known energies we can extract a best fit for the value of the gains (g_1, g_2) by making a Doke plot [ref]. The mono energetic lines used for the purposes of the calibration are listed in table 1. For each calibration point we plot the mean S_1/E vs. mean S_2/E (Equation 3) and fit a line, the x and y intercepts (Equation 4) yields the value of g_1/W and g_2/W respectively. The value of the work function W in liquid xenon has been found to be 0.0137 ± 0.002 [ref]. The values of g_1, g_2 are degenerate and highly correlated such that the ratio of $g_1:g_2$ is always a constant, a reduction in g_1 can be compensated by an increase in g_2 and still yield the same number of initial quanta and visa versa. Breaking the degeneracy requires data over a wide range of S_1 and S_2 values near the intercept of the Doke plot. Due to the strong correlation in the fit parameters the data is fit by minimizing the likelihood and the errors in intercept and slope are determined using MCMC (Markov Chain Monte Carlo).

$$\begin{aligned}\langle n_\gamma \rangle &= \frac{\langle S_1 \rangle}{g_1} \\ \langle n_e \rangle &= \frac{\langle S_2 \rangle}{g_2}\end{aligned}\tag{2}$$

$$\begin{aligned}S_1/E &= \frac{n_\gamma}{(n_\gamma + n_e)} \times \frac{g_1}{W} \\ S_2/E &= \frac{n_e}{(n_\gamma + n_e)} \times \frac{g_2}{W}\end{aligned}\tag{3}$$

$$\begin{aligned}1 &= \left(\frac{S_1}{E}\right) \left(\frac{W}{g_1}\right) + \left(\frac{S_2}{E}\right) \left(\frac{W}{g_2}\right) \\ \left(\frac{S_1}{E}\right) &= \left(\frac{g_1}{W}\right) - \left(\frac{S_2}{E}\right) \left(\frac{g_1}{g_2}\right) \\ y = \frac{S_1}{E}, x = \frac{S_2}{E}, y &= m \cdot x + b \\ g_1 &= b \cdot W \\ g_2 &= \frac{g_1}{m} = \frac{b \cdot W}{m}\end{aligned}\tag{4}$$

1.1 Anti-Correlation Space

The first step in calibrating the energy scale is to plot the observables S_1 vs. S_2 , by doing this the anti correlation between light and charge at a given energy become apparent, figure 2.

Source	Energy [keV]	Decay Type
Xe K shell	29.7, 34	X-ray
^{83m}Kr	41.55**	Internal Conversion
^{131}Xe	163.9	Internal Conversion
^{127}Xe	203 or 375	^{127}I daughter γ -emission
	33.8	Kb shell X-ray
	5.3	L shell X-ray
^{129m}Xe	236.1	Internal Conversion
^{214}Bi	609	Inverse Beta Decay
^{137}Cs	661.6	Photo-absorption

Table 1: Mono energetic peaks used for g1 g2 calibration. ** Kr83 data was taken at 50 and 105 [V/cm] along with the standard field of 180 [V/cm].

For the data presented here a fiducial cut was placed at a radius of less than 18 [cm] and drift distance between 6 and 46 [cm] which greatly reduces the background event rate. To extract g1 g2 we first determine the average values of S1 and S2 at each known energy. Initially loose diagonal cuts are placed by eye on the populations, figure 2. Next, using a un-binned maximum likelihood fit the mean and sigma are estimated and then refit using $\pm 2\sigma$ of the initial distribution to remove tails from backgrounds. With the initial estimate for the mean S1 and S2 response to a given energy the gains g1,g2 are determined. The resulting value of g1 and g2 is found to be 0.096 ± 0.009 and 5.94 ± 1.68 respectively, the fit is shown in figure 3. The values of g1 and g2 represent a best fit tot he underling recombination theory where for each additional photon there is a corresponding reduction of one electron and visa versa. The method for extracting the uncertainties using MCMC will be discussed later in section 1.3.

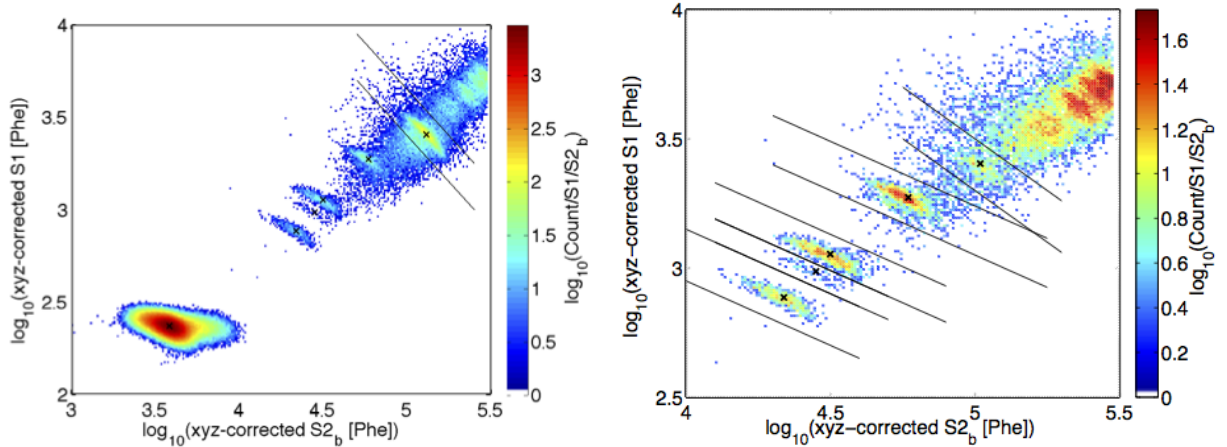


Figure 2: LUX data in anti correlation space (S1 vs. S2), the black lines indicate the initial cuts by eye used to isolate populations of constant energy. In both figures diagonals represent lines of constant energy with a slope depending on the local recombination probability. The centroids found by an unbinned maximum likelihood analysis are shows as a black X, for sources show in table 1.

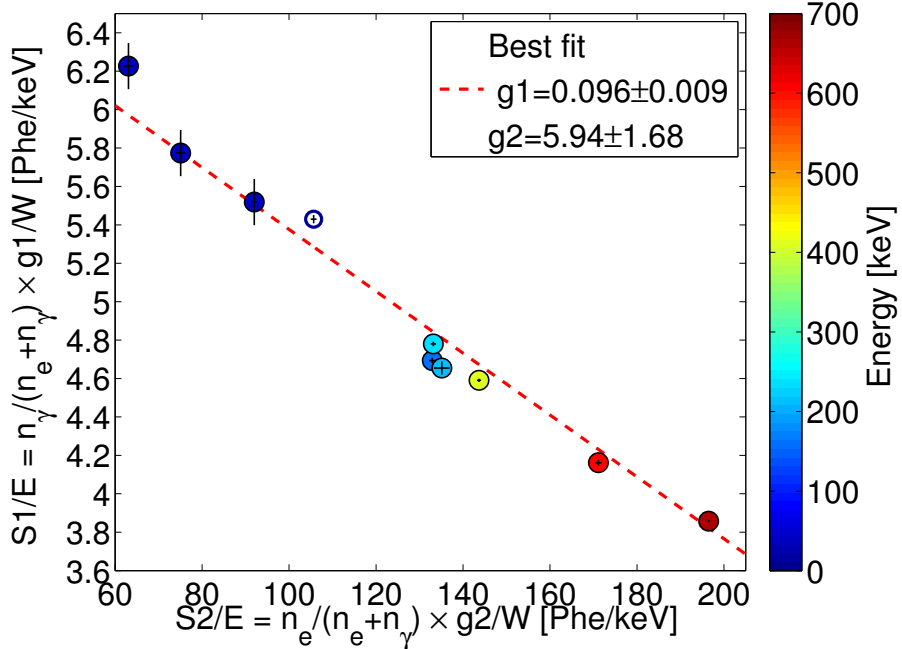


Figure 3: Doke plot showing the best fit for the energy calibration parameters g_1 and g_2 using S_1 and S_2 means extracted from anti-correlation space. The first three blue points, from the left, are from ^{83}Kr calibrations at 50, 105 and 180 V/cm respectively. The open circle was from the K-shell xenon X-ray and was not used for the fit as it's absolute energy and origin from the skin of the detector is uncertain.

1.2 Refitting in Combined Energy Space

From the first attempt to find g_1, g_2 we see, in figure 3, that there are discrepancies between the data and the fit, however this first result is only a crude estimate derived from anti correlation space. Once we have an initial estimate of gains g_1, g_2 a combined energy scale can be constructed with significantly improved resolution over the initial guess, due to the fact that recombination fluctuations are canceled. With the improved resolution the data are fit around the combined energy peaks using an unbinned maximum likelihood fit to a normal distribution, and then the data refitted around 1.5σ of the initial fit. The fits used to extract the means and sigmas of the S_1 and S_2 signals at a given energy are show in figures 5 and 6. We iterate this technique twice as the convergence is rapid, in this case the initial value of g_1 and g_2 derived from anti-correlation space are already a close approximation to the true value. The resulting value of g_1 and g_2 is found to be 0.097 ± 0.008 and 5.75 ± 1.4 respectively, the fit is shown in figure 4. After refitting there is a significant improvement over figure 3, especially the xenon activation lines in the center, which is due to better peak finding in combined energy space over anti-correlation space.

$$\begin{aligned} g_1 &= 0.097 \pm 0.008 \\ g_2 &= 5.75 \pm 1.4 \end{aligned} \tag{5}$$

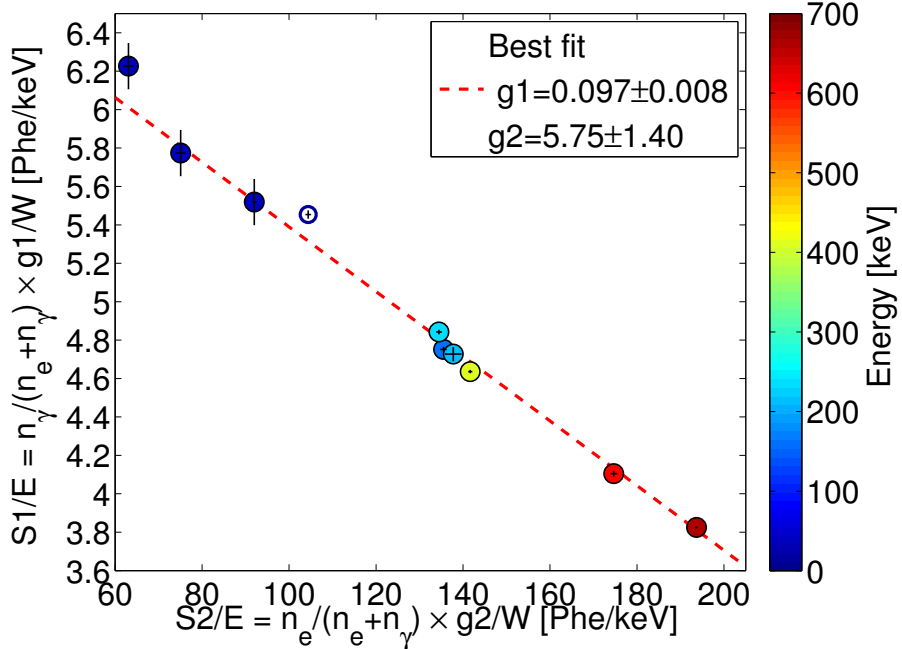


Figure 4: Doke plot showing the best fit for the energy calibration parameters g_1 and g_2 using S_1 and S_2 extracted from a combined energy space. The first three blue points, from the left, are from ^{83}Kr calibrations at 50, 105 and 180 V/cm respectively. The open circle was from the K-shell xenon X-ray and was not used for the fit as it's absolute energy and origin from the skin of the detector is uncertain.

Figure 7 is the final Doke plot for multiple peaks the theory describes the data well using the optimal fit for g_1 and g_2 , for each increase in number of photons there is a corresponding decrease in the number of electrons and visa versa. The relatively large error on g_2 is due to the distance of the data points from the x-intercept. As stated before the values of g_1 and g_2 can be locally degenerate as long as their ratio remains a constant. Thus for future studies it will be important to probe more of the parameter space in order to place a tighter constraint on gains g_1 and g_2 .

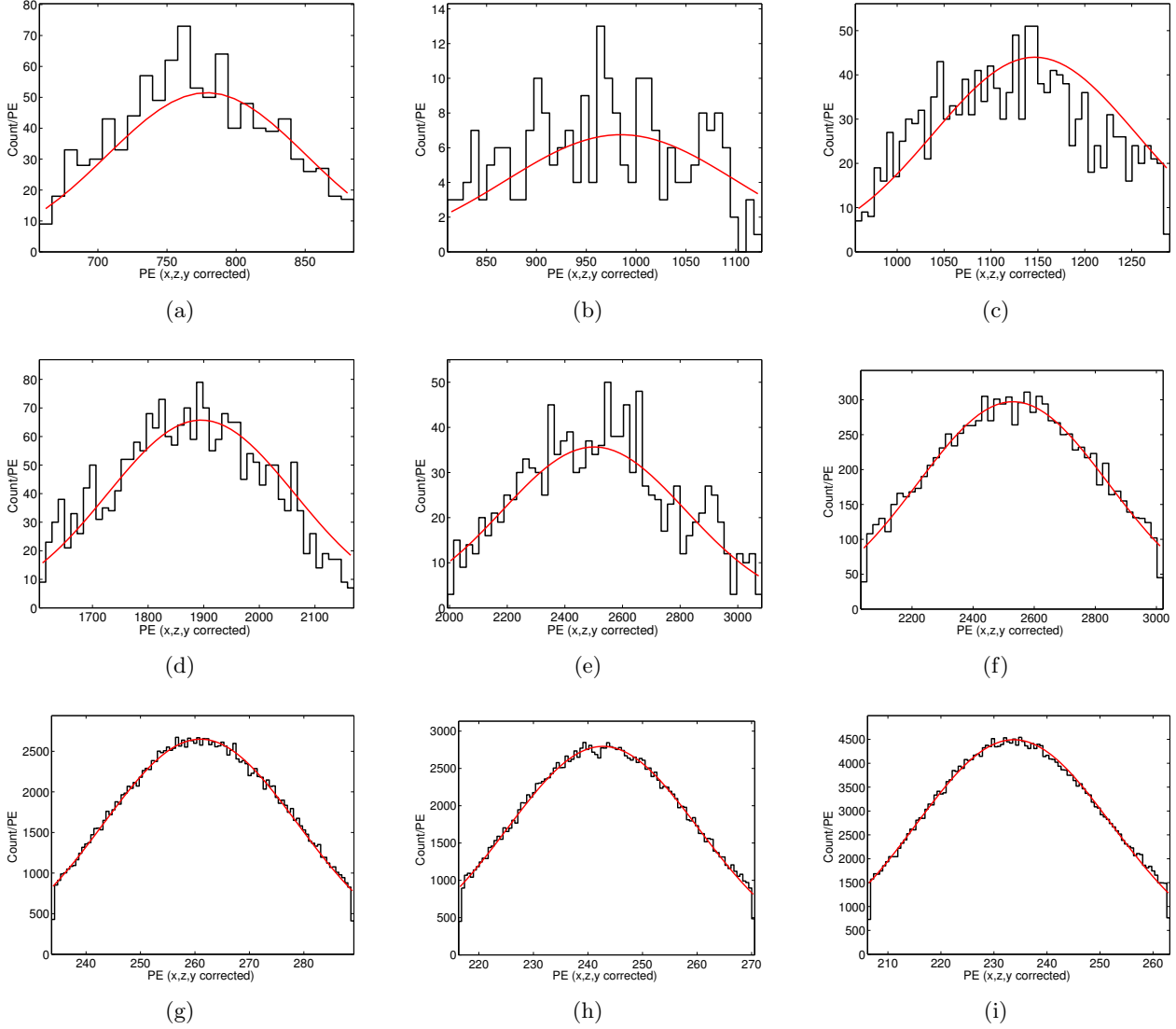


Figure 5: S1 fits to sources at nominal field of 180 [V/cm] unless otherwise noted. Source and energy in keV from top left to bottom right: a) ^{131}Xe : 163, b) ^{127}Xe : 207, c) ^{127}Xe & $^{129\text{m}}\text{Xe}$: 236.8, d) ^{127}Xe : 410, e) ^{214}Bi : 609, f) ^{137}Cs : 661.6, g) $^{83\text{m}}\text{Kr}$: 41.5 - at 50 [V/cm], h) $^{83\text{m}}\text{Kr}$ 41.5 - at 105 [V/cm], i) $^{83\text{m}}\text{Kr}$ 41.5 .

1.3 Finding Errors with MCMC

The error bars reported in this section on $g1$ and $g2$ are from the error in the slope and intercept of the linear fit in the Doke plot derived using MCMC. For calculating the error in slope and intercept three random walkers were used at each data point and allowed to take 500 steps. The MCMC takes into account the covariance of the parameters, shown in figure 8 as a two dimensional Gaussian. There is a strong negative correlation between the slope m and intercept b which is the result of the degeneracy between gains $g1$ and $g2$ used to reconstruct energy by combining the light and charge signal. Thus, the error on $g1$ and $g2$

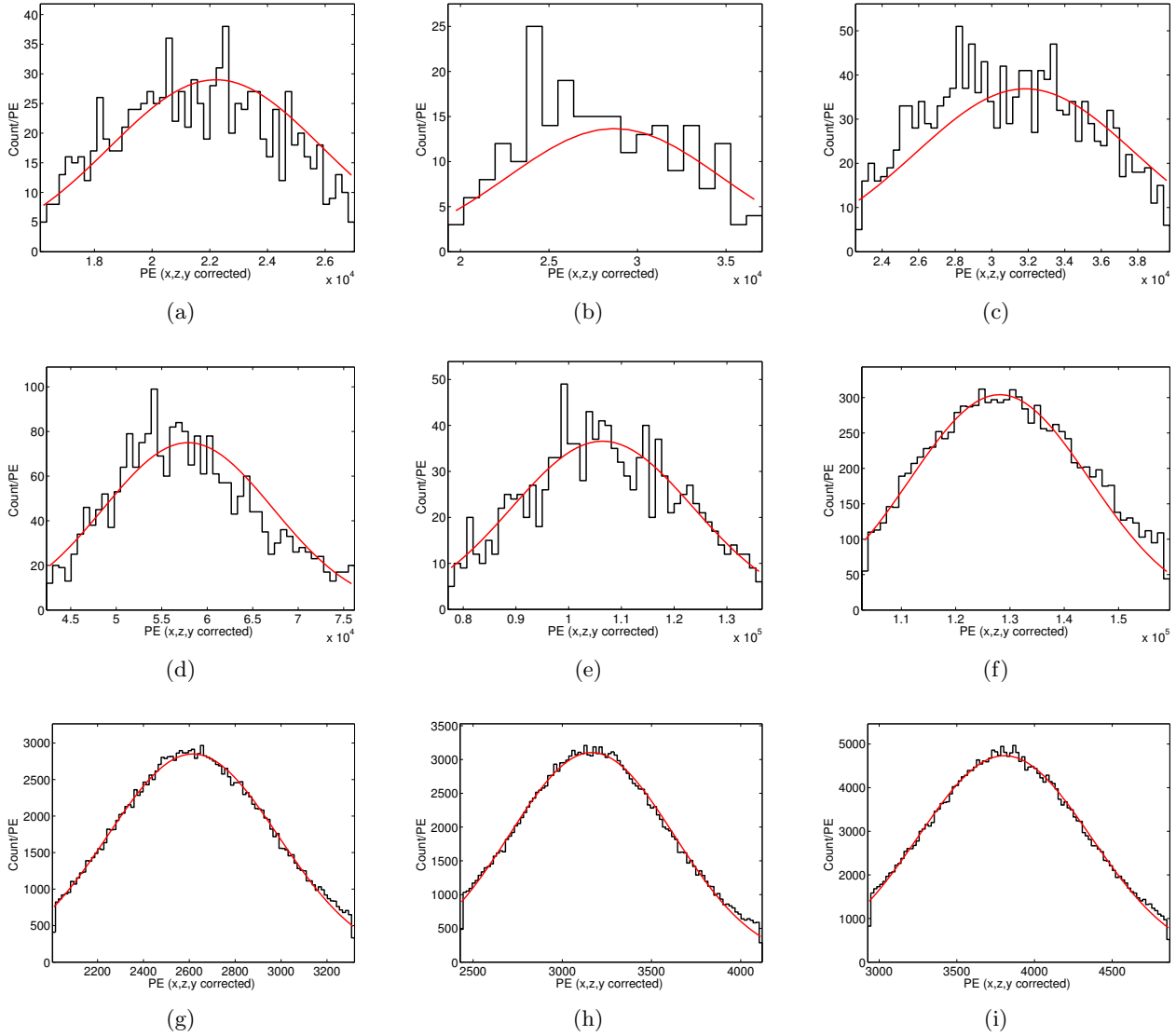


Figure 6: S2 fits to sources at nominal field of 180 [V/cm] unless otherwise noted. Source and energy in keV from top left to bottom right: a) ^{131}Xe : 163, b) ^{127}Xe : 207, c) ^{127}Xe & $^{129\text{m}}\text{Xe}$: 236.8, d) ^{127}Xe : 410, e) ^{214}Bi : 609, f) ^{137}Cs : 661.6, g) $^{83\text{m}}\text{Kr}$: 41.5 - at 50 [V/cm], h) $^{83\text{m}}\text{Kr}$ 41.5 - at 105 [V/cm], i) $^{83\text{m}}\text{Kr}$ 41.5 .

is such that for the positive maxima deviation in g1 we reach the negative maxima of the error on g2, and visa versa. Using standard reduced χ^2 for fitting and calculating errors in the slope and intercept would be underestimated the true error by a factor of five as it does not account for the degeneracy of the anti-correlated gains.

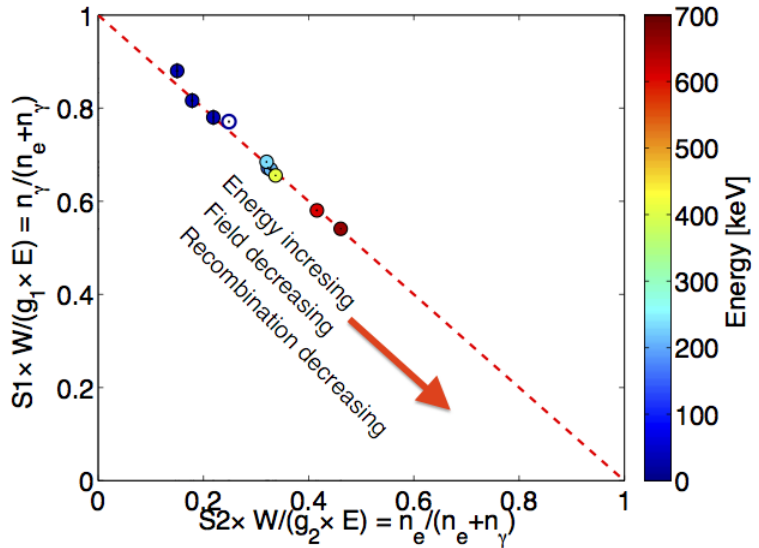


Figure 7: Doke plot of the data showing the light yield vs. charge yield. Only solid circles are used for the fit, the open circle is the Xe K shell X-ray from the detector edge.

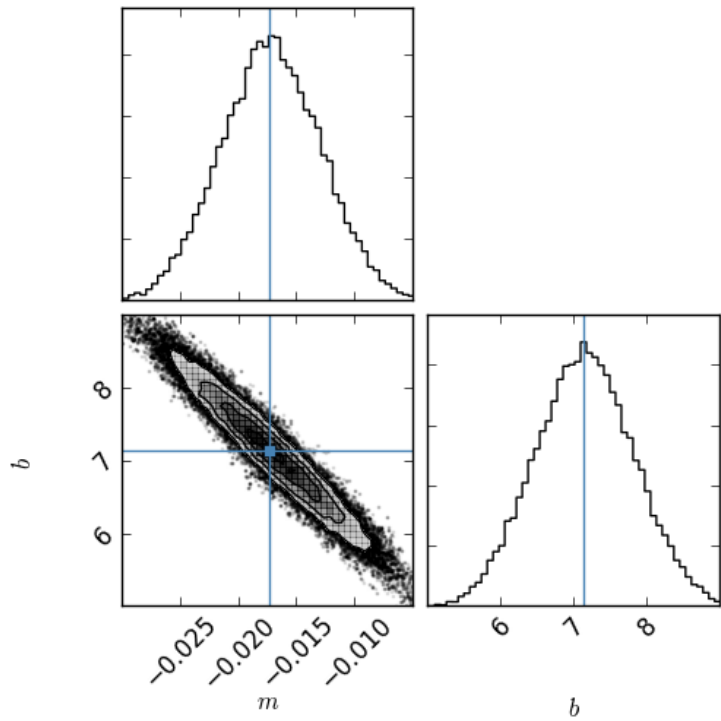


Figure 8: MCMC for the linear fit to the Doke plot. There is a strong negative correlation between the slope m and intercept b which results from the degeneracy between gains g_1 and g_2 .

1.4 Combined Energy Space

With the values of g_1 and g_2 known the combined energy of events can be reconstructed with a significant improvement over using only the light or charge channel. In combined energy space recombination fluctuations are removed by the anti correlation of light and charge production and any residual smearing is due to intrinsic detector resolution (discussed later in section :). Figure 9 shows the energy histograms of the data used for the fits to gains g_1 and g_2 including the xenon activation lines and the ^{137}Cs calibration, along with a zoom in of the xenon K shell Xray at 34 keV and a 81 keV gamma from ^{133}Xe , not used for finding g_1, g_2 . With the energy scale calibrated we can now reconstruct the energy of the events and convert the measured S1 and S2 signals to fundamental quanta using the gains g_1, g_2 allowing us to untangle instrumental and recombination fluctuations and measure light and charge yields.

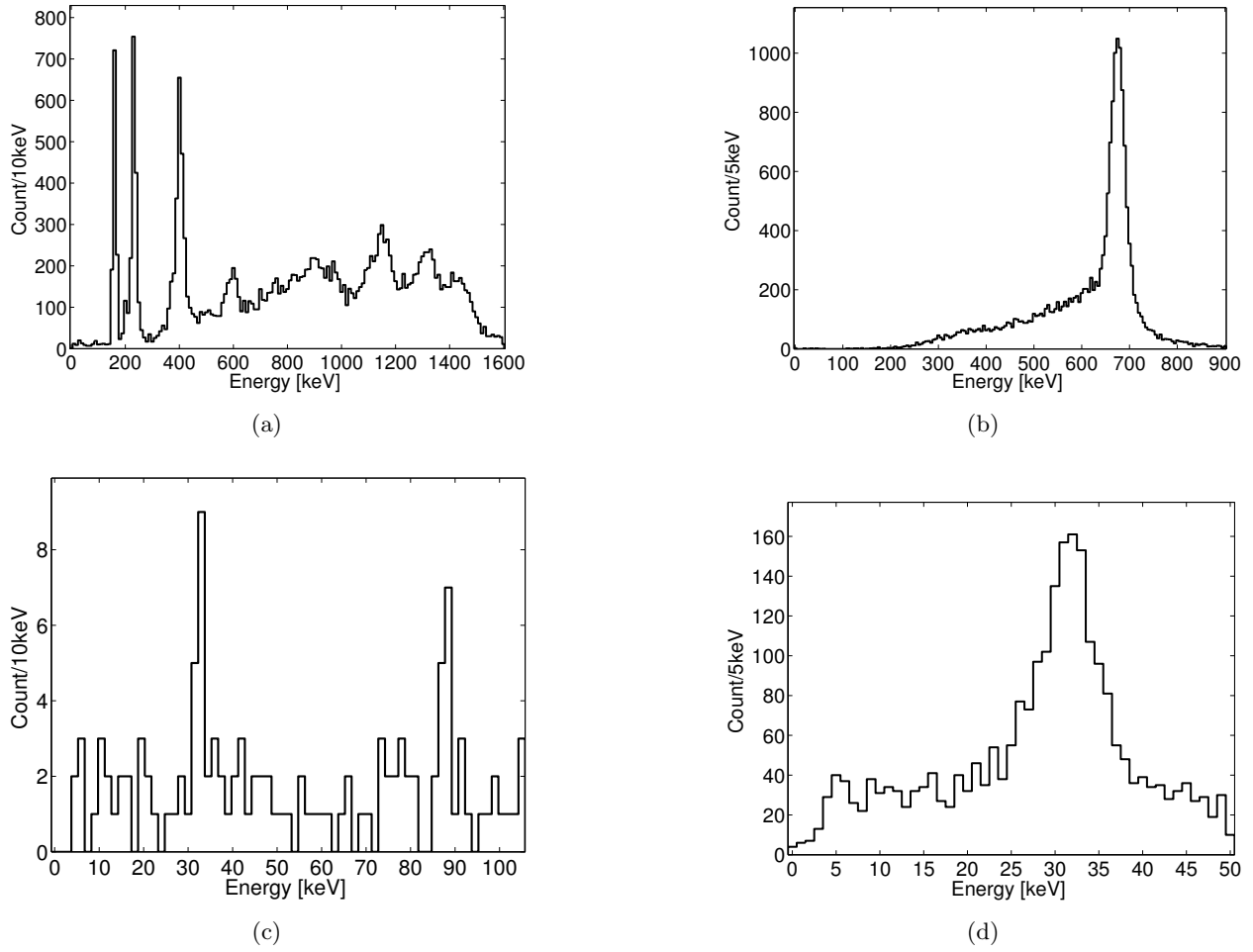


Figure 9: Combined energy scale. a) The xenon activation lines from early in the run. b) ^{137}Cs calibration data. c) Xenon X-ray from the teflon skin (radium cut increased to the detector edge). d) Xenon X-ray and ^{133}Xe at 81 keV, due to low stats was not used for fitting.

1.5 Light Collection and Electron extraction

The value of g_1 represents the mean efficiency for collecting photons at the center of the LUX detector, the response to S1 light is flat fielded and normalized to the detector center (section Kr calibrations). The measured value of $g_1 = 0.097 \pm 0.008$ implies a 9.7% probability of a photon propagated from the center of the detector striking a PMT and being converting into a photo electron (PE) signal. The value of g_2 represents the average number of PE collected for each electron that escaped recombination at the initial interaction site then drifted by the electric field towards liquid-gas interface where it is extracted. Note, S2 signals are corrected for depth as impurities exponentially attenuate electrons drifting through the xenon (section Kr cal). Due to electro-luminescence the S2 signal is such that a single extracted electron creates tens of photons which are collected by both PMT arrays. In our analysis we can cut on the single electron population (small S2 pulses without an associated S1) and measure the single electron size along with the extraction efficiency efficiency. The extraction efficiency is defined as the probability that an electron will be extracted from the liquid into the gas in a region of 3.5 kV between the anode and the gate. For a given event the extraction of electrons is a binomial processes with a rate approaching unity for fields above 5 kV (reference). Figure 10, shows the single electron size as measured by the bottom PMT array (used for S2 pulses in the LUX detector to avoid saturation). The population is modeled by a skew Gaussian due to the Poisson nature of measuring only a handful of photo electrons (PE) per extracted electron. The mean of the distribution is found to be 9.7 PE/e^- with a width of $\sigma_{\text{SE}} = 3.6 \text{ Phe/e}^-$. Thus, the extraction efficiency is g_2 over the single electron size 59.3%, which given the extraction field is in good agreement measurements in other xenon detectors -[2 refs extraction].

2 Modeling Intrinsic Detector Resolution

Intrinsic statistical fluctuations in light and charge (S1, S2) collection in the LUX detector lead to a spread in collected quanta. To measure effects from recombination fluctuations and the Fano factor we must first decouple the detector component of resolution. We use the model described in [Dahl's thesis] in which the measured scintillation and ionization signals S1, S2 (measured in Phe) are related to the number of photons and electrons by gains g_1 and g_2 , 6. Specifically, the average number of photons and electrons produced for a given energy deposit are proportional to the average S1,S2 signals at a given drift field. The gain g_1 represents photon detection efficiency, the probability of a photon from an energy deposit striking a PMT convolved with the quantum efficiency of the PMTs. Gain g_2 represents the average S2 signal of a single electron normalized by the average single electron size. Where S2 uses only the bottom PMT array and is corrected for lifetime.

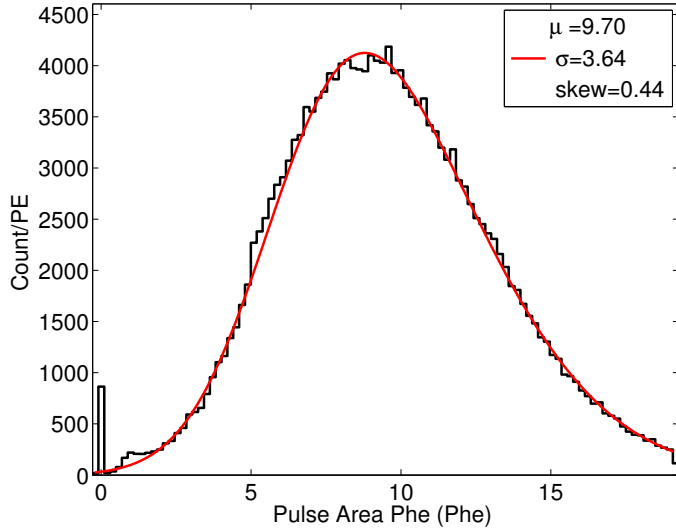


Figure 10: Single electron distribution as seen by the bottom PMT array fitted with a skew Gaussian model to account for the underlying Poisson statistics of observing between 9 and 10 photo electrons (PE) for each electron leaving the liquid and entering to the gas phase at a higher field causing electro-luminescence. The μ of the fit represents the true mean of the skew Gaussian distribution.

$$\begin{aligned}\langle n_\gamma \rangle &= \frac{\langle S1 \rangle}{g_1} \\ \langle n_e \rangle &= \frac{\langle S2 \rangle}{g_2}\end{aligned}\tag{6}$$

The statistical fluctuations for the measured number of quanta in equation 6 are from the statistical processes that comprise the measured S1 and S2 signal.

$$\begin{aligned}\sigma_{n_{\gamma_{\text{stat}}}}^2 &= \frac{\sigma_{S1_{\text{stat}}}^2}{g_1^2} \\ \sigma_{n_{e_{\text{stat}}}}^2 &= \frac{\sigma_{S2_{\text{stat}}}^2}{g_2^2}\end{aligned}\tag{7}$$

The variance in the number of photons in equation 7 can be broken into two parts. First, a binomial variance due to counting a fraction, g_1 , of the initial photons produced. $\text{Var}_{n_\gamma} = \frac{(1-g_1) \times g_1 \times n_\gamma}{g_1^2}$. Second, the variance in the response of the PMTs to a single photon. $\text{Var}_{n_\gamma} = \frac{g_1 \times n_\gamma \times \sigma_{\text{PE}}^2}{g_1^2}$. Combining the two leads to the result in equation 8.

$$\sigma_{n_{\gamma_{\text{stat}}}}^2 = \frac{1 - g_1 + \sigma_{\text{PE}}^2}{g_1} n_\gamma\tag{8}$$

The variance in the number of electrons in equation 7 is comprised of the following statistical uncertainties. First, a binomial variance due to the extraction efficiency of electrons from the liquid-gas interface. $\text{Var}_{n_e} = \frac{(1-\text{ext}) \times \text{Ext} \times n_e \times (\text{single}_E)}{g_2^2}$, Ext is the electron extraction probability and single_E is the single electron size in PE. Second, the variance in the response of the PMTs to a single electron. $\text{Var}_{n_e} = \frac{\text{Ext} \times n_e \times \sigma_{\text{SE}}^2}{g_2^2}$. Finally, the additional variance from electron attenuation is modeled as a Poisson probability of electron capture in each Z slice of the detector. The variance from each Z slice depends of the average number of electrons that will be attenuated. The probability of attenuation at each slice in drift time T is $P(T) = 1 - e^{-T/\tau}$, where τ for the data sets to be considered is 1000 μs . The drift region considered in the fiducial volume is from 38 to 304.5 μs . The average variance from events in the fiducial can be given by equation 9.

$$\sigma_{n_{e_{\text{att}}}}^2 = n_e \frac{\int_{T_{\text{min}}}^{T_{\text{max}}} (1 - e^{-T/\tau}) dT}{\int_{T_{\text{min}}}^{T_{\text{max}}} dT} = 0.155 \times n_e \quad (9)$$

Combining the variances leads to the result for the statistical variance in the observed number of electrons equation 10.

$$\sigma_{n_{e_{\text{stat}}}}^2 = \frac{\text{Ext} \times \sigma_{\text{SE}}^2 + (1 - \text{Ext}) \times g_2^2}{g_2^2} n_e + \sigma_{n_{e_{\text{att}}}}^2 \quad (10)$$

For this analysis we use the following detector gains, given measured by comparing tritium data to the vetted region of LUXSIM (S1 between 7-50 Phe) 11.

$$\begin{aligned} g_1 &= 0.097 \pm 0.008 [\text{Phe}/n_\gamma] \\ g_2 &= \text{SE}_b \times \text{Ext} = 5.75 \pm 1.4 [\text{Phe}/n_e] \\ \text{SE}_b &= 9.70 \pm 0.05 [\text{Phe}/n_e] \\ \sigma_{\text{SE}_b} &= 3.64 [\text{Phe}/n_e] \\ \text{Ext} &= 0.593 \pm 0.144 \\ \sigma_{\text{PE}} &= 0.51 [\text{Phe}/n_\gamma] \end{aligned} \quad (11)$$

Combining equations 8-11 we find the intrinsic detector resolution for the average S1 and S2 signals in the LUX detector, equation 12. Note, the intrinsic resolution in S2 is subdominant to that of S1, since on average one electron multiplies to about ten photons detected by the bottom PMT array [ref]. Also listed in 13, are the instrumental fluctuations with a linear dependance on quanta measured with a global fit to mono energetic sources

[next section]. The total variance in the light and charge channels is the linear combination of the statistical and instrumental variance.

$$\begin{aligned}\sigma_{n_{\gamma_{\text{stat}}}} &= 3.46\sqrt{n_{\gamma}} \\ \sigma_{n_{e_{\text{stat}}}} &= 0.68\sqrt{n_e}\end{aligned}\tag{12}$$

$$\begin{aligned}\sigma_{n_{\gamma_{\text{inst}}}} &= \frac{6.4 \pm 1.7}{100} \times n_{\gamma} \\ \sigma_{n_{e_{\text{inst}}}} &= \frac{6.6 \pm 0.9}{100} \times n_e\end{aligned}\tag{13}$$

3 Measuring Recombination Fluctuations

3.1 Measuring Recombination Fluctuations with Mono-Energetic Sources

To model recombination we start with a basic assumption that for a given energy deposit in liquid xenon the number of quanta produced is equal to the number of exitons and the number of ions. The number of ions generated contains a spread given by a Fano factor F . The value of F for liquid xenon is small, has a theoretical value of 0.05 [3].

$$\begin{aligned}\frac{E}{W} &= n_q = n_i + n_{ex} \\ \frac{E}{W} &= n_{\gamma} + n_e\end{aligned}\tag{14}$$

Where E is energy in [keV], W is the work function in [keV/quanta], n_q is the number of quanta, n_i is the number of ions and n_{ex} is the number of exitons. The theoretical value of the number of exitons produced to ions is $\frac{n_{ex}}{n_i} = \alpha = 0.06$ and is not expected to change vs. energy [ref]. For the subsequent equations in this section we will simplify equations 14 to that in 15.

$$\begin{aligned}\alpha &= 0.06 \\ n_i &= \frac{E}{W} \frac{1}{(1 + \alpha)} = \frac{n_{\gamma} + n_e}{(1 + \alpha)} \\ \sigma_{n_i}^2 &= F \times n_i\end{aligned}\tag{15}$$

Equation 15 gives us a simple model for the number of ions and exitons produced for a given interaction, the only spread in quanta thus far is due to a Fano factor governing the spread in initial quanta produced. We now convert ions and exitons to scintillation and ionization signals that are measured in the LUX detector, S1 and S2 respectively. Photons resulting from an energy deposit arise from the exitons that de-excite and from ions which

recombine with freed electrons. The number of electrons corresponding to the energy deposit will be equal to the number of ions that did not recombine with a freed electron.

$$\begin{aligned} n_\gamma &= n_{\text{ex}} + n_i \times r = n_i \times (r + \alpha) \\ n_e &= n_i \times (1 - r) \\ r &= \frac{\frac{n_\gamma}{n_e} - \alpha}{\frac{n_\gamma}{n_e} + 1} \end{aligned} \quad (16)$$

Where r represents the electron-ion recombination probability. A key measurable quantity is the size of recombination probability fluctuation σ_r . Since we measure n_γ and n_e as S1 and S2 signals and not ions and exitons, an additional variance arises from the ion-electron recombination fluctuations. These recombination fluctuations are dependent on the dE/dx of each individual electron produced making them much larger than the spread from the Fano factor. We now combine the uncertainties from the Fano factor, recombination and the statistical uncertainty from detector resolution (σ_{Det}) and solve for the observed quantities given in 17:

$$\begin{aligned} \sigma_{n_\gamma}^2 &= \sigma_{n_{\text{ex}}}^2 + \sigma_{n_i}^2 r^2 + \sigma_r^2 n_i^2 + \sigma_{n_{\gamma\text{Det}}}^2 = \sigma_{n_{\text{ex}}}^2 + n_i F(r^2) + \sigma_r^2 n_i^2 + \sigma_{n_{\gamma\text{Det}}}^2 \\ \sigma_{n_e}^2 &= \sigma_{n_i}^2 (1 - r)^2 + \sigma_r^2 n_i^2 + \sigma_{n_{e\text{Det}}}^2 = n_i F(1 - r)^2 + \sigma_r^2 n_i^2 + \sigma_{n_{e\text{Det}}}^2 \end{aligned} \quad (17)$$

For convenience we will work with $n_i = (n_\gamma + n_e)/(1 + \alpha)$, this convention is chosen because both the Fano factor and recombination fluctuations act on number of ions and also because the number of ions are linearly related to the initial energy deposit. Using a mono energetic source and combined energy(equation 14) we can measure $\sigma_{n_\gamma}^2$ and σ_e^2 and σ_E^2 . Dropping the contribution form the Fano factor and the the number of exitons it can be shown that the value recombination fluctuations σ_R can be determined by rearranging equation 17, keeping in ming that σ_E contains no recombination fluctuations. Where σ_R is in units of quanta, $\sigma_R = n_i \sigma_r$.

$$\sigma_R^2 = \frac{1}{2} \left(\sigma_{n_\gamma}^2 + \sigma_{n_e}^2 - \frac{\sigma_E^2}{W^2} \right) \quad (18)$$

Where the spread in observed quanta $\sigma_{n_\gamma}^2$ and $\sigma_{n_e}^2$ result from a linear combination of the variance from detector resolution and recombination fluctuations.

$$\begin{aligned} \sigma_{n_\gamma}^2 &= \sigma_{n_{\gamma\text{Det}}}^2 + \sigma R^2 \\ \sigma_{n_e}^2 &= \sigma_{n_{e\text{Det}}}^2 + \sigma R^2 \end{aligned} \quad (19)$$

We do not directly observe the fluctuation in number of photons and electrons, instead we measure the fluctuations in the corresponding S1 and S2. The fluctuation in the S1 and S2 signal when divided by the gains g1 g2 represent on average the fluctuation in photons or

electrons due to detector resolutions (statistical and instrumental variance) combined with recombination fluctuations. 19.

$$\begin{aligned}\sigma_{n_{\gamma\text{Det}}}^2 &= \frac{\sigma_{S1}^2}{g_1^2} - \sigma R^2 \\ \sigma_{n_{e\text{Det}}}^2 &= \frac{\sigma_{S2}^2}{g_2^2} - \sigma R^2\end{aligned}\quad (20)$$

Combining equations 18 and 20 leads to the results in equation 21, which is a formula to directly measure recombination fluctuations using a mono energetic source.

$$\sigma_R^2 = \frac{1}{2} \left(\frac{\sigma_{S1}^2}{g_1^2} + \frac{\sigma_{S2}^2}{g_2^2} - \frac{\sigma_E^2}{W^2} \right) \quad (21)$$

Equations 21 and 20 gives us a method to measure recombination fluctuations along with fluctuations in n_γ and n_e due to intrinsic detector resolution, (will be discussed in the next section). It is important to note that $\sigma_{n_\gamma}^2$, $\sigma_{n_e}^2$ and σ_E^2 are observable quantities when using a mono energetic source. The variance in combined energy does not contain variance from recombination fluctuations as those fluctuation occur along lines of constant energy. Note, we have dropped the contribution from the Fano factor and the spread is exitons as they are much smaller than recombination fluctuations or the variances from measuring light and charge intrinsic to the detector. The observed variance in the light and charge channels (S1, S2) is the result of two compounded random processes. After the initial charge deposit the number of charge and light quanta undergo recombination fluctuations. Subsequently, as the light or charge is collected in the detector an additional variance from detector resolution occurs. The result is the sum of two random processes thus the variance are added.

3.2 Results with Mono Energetic Calibration Sources

Using equation 21 and 20 along with the measurements of $g1$ $g2$, we construct a combined energy and deconvolve the recombination fluctuations from variances in the light and charge channel of the detector. The result is shown in figure 11, the black white and red lines represent σ_R , $\sigma_{n_{\gamma\text{Det}}}$, $\sigma_{n_{e\text{Det}}}$, respectively for sources listed in Table 1. A variance with a linear and root term is fit to the data and used to extract instrumental fluctuations and constrain the statistical fluctuations. The linear term corresponds to instrumental fluctuations and the root term corresponds to statistical fluctuations. Instrumental fluctuations go like the signal size and may potentially be due to ripples in the liquid surface caused by xenon bubbles or other systematics that are unaccounted for. The root term should result purely from counting photo electrons, described earlier. We find:

$$\begin{aligned}\sigma_{n_{\gamma\text{Det}}}^2 &= \sigma_{n_{\gamma\text{Stat}}}^2 + \sigma_{n_{\gamma\text{Inst}}}^2 = (0 \pm 10 \cdot \sqrt{n_\gamma})^2 + ((6.4 \pm 1.8)/100 \cdot n_\gamma)^2 \\ \sigma_{n_{e\text{Det}}}^2 &= \sigma_{n_{e\text{Stat}}}^2 + \sigma_{n_{e\text{Inst}}}^2 = (1 \pm 4 \cdot \sqrt{n_e})^2 + ((6.6 \pm 0.6)/100 \cdot n_e)^2 \\ \sigma_R^2 &= ((5.5 \pm 0.5)/100 \cdot n_q)^2\end{aligned}\quad (22)$$

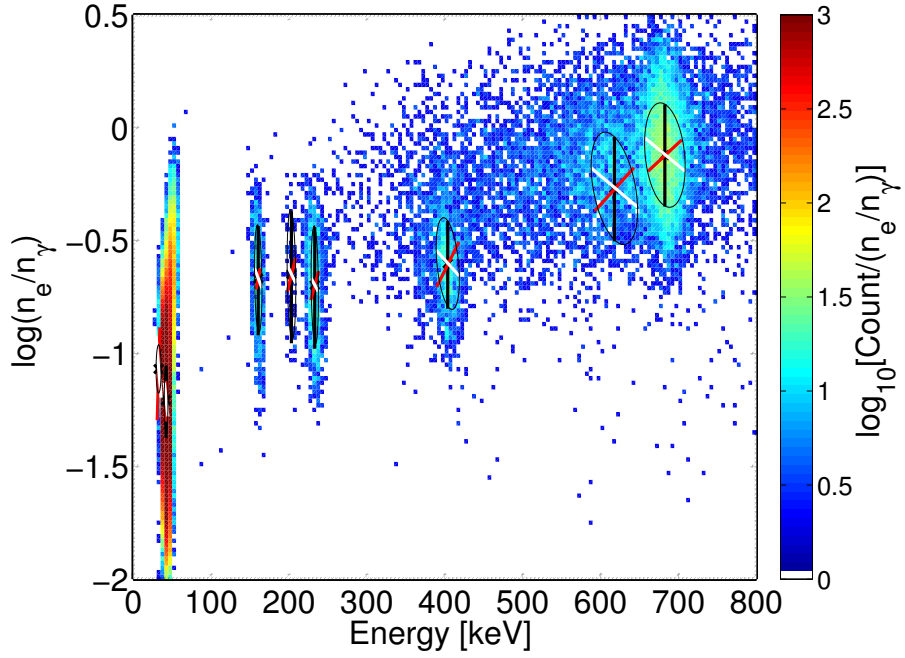


Figure 11: Populations of calibration sources in discrimination space $\log\left(\frac{n_e}{n_\gamma}\right)$ vs. combined energy [keV_{ee}]. The ovals represent the combination of σR , $\sigma n_{\gamma_{\text{Det}}}$, $\sigma n_{e_{\text{Det}}}$ in black, white, red respectively.

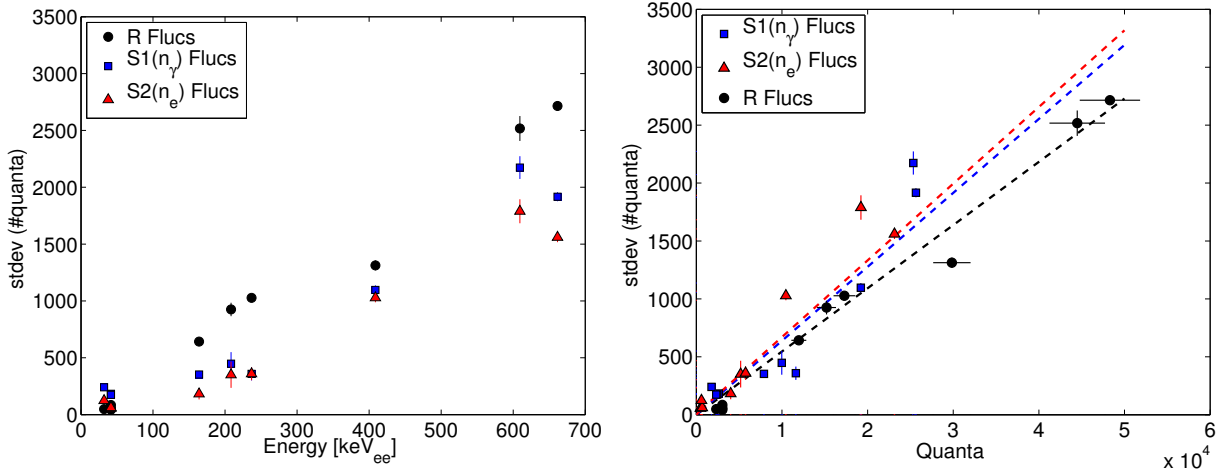


Figure 12: Measured values of σR , $\sigma n_{\gamma_{\text{Det}}}$, $\sigma n_{e_{\text{Det}}}$ vs. Energy on the left and vs. Quanta on the right. Measured using sources listed in Table 1.

3.3 Measuring Recombination Fluctuations in Desecrate Energy Bins

The pervious subsection demonstrated the power of using a mono energetic source measure recombination fluctuations, equation 18. In this section we present a method to decouple statistical variance from recombination fluctuations when confined to an energy bin of width Δ_E . The consideration of desecrate binning is crucial when dealing with a continual energy spectrum. Take the tritium beta spectrum as an example, we lose the ability to independently measure $\sigma_{n_\gamma}^2$, $\sigma_{n_e}^2$, σ_E^2 and are only left with a smear of n_γ , n_e , E . However, there are two key pieces of information still left at our disposal. First, the combined energy can be reconstructed from global fits to g1 and g2, and even corrected for spectral shape and detector resolution (discussed later in section [link]). Second, we can calculate values of statistical variance for the light and charge channels as a function of energy, described in 12, 13. It will be shown in this section that having a priori knowledge of g1,g2 and the functional for of the statistical variance from detector resolution will be sufficient to measure recombination fluctuations for a continual energy spectrum binned in energy with width Δ_E .

We begin the treatment of binning with the the case of having a finite bin width around the central combined energy of a mono energetic source. First, we quantify the change in the statistical components of equation 17 when slicing out a bin in combined energy space. The slice in combined energy is illustrated for a toy model at quanta corresponding to that of the combined 41.6 keV ^{83}Kr decay in Figure 13. All contribution from recombination fluctuations are included when slicing out a section of combined energy, illustrated in Figure 13. However, the slice contains only a reduced statistical component from both the light and charge signals, and in the limit that ΔE goes to zero the statistical component of light and charge converge to a value defined as χ_{stat} (where χ is the measured σ in a bin of combined energy). To solve for the value of χ_{stat} we first calculate the slope induced by statistical variance in the number of photons vs. quanta and the complementary slope of electrons vs. quanta, defined as M and 1-M respectively. The value of M depends on the magnitude of the statistical variances and is given in equation 23. The sum of the two slopes must equal one as the sum of photons and electors make up combined energy.

$$\begin{aligned} M &= \tan(\theta_{n_{\gamma\text{Det}}}) = \frac{\sigma_{n_{\gamma\text{Det}}}^2}{\sigma_{n_{\gamma\text{Det}}}^2 + \sigma_{n_{\gamma\text{Det}}}^2} \\ 1 - M &= \tan(\theta_{n_{e\text{Det}}}) = \frac{\sigma_{n_{e\text{Det}}}^2}{\sigma_{n_{\gamma\text{Det}}}^2 + \sigma_{n_{\gamma\text{Det}}}^2} \end{aligned} \quad (23)$$

With the slope between combined energy and $\sigma_{n_{\gamma\text{Det}}}$ and between energy and $\sigma_{n_{e\text{Det}}}$ defined in equation 23 the value of the shared statistical uncertainty in combined energy space can be determined. We first treat the case of $\Delta E = 0$ in equation 24 which is also valid when the centroid of light yield and charge yield has been subtracted (discussed later).

$$\chi_{\text{Det}}^2 = M^2 \sigma_{n_{e\text{Det}}}^2 + (1 - M)^2 \sigma_{n_{\gamma\text{Det}}}^2 \quad (24)$$

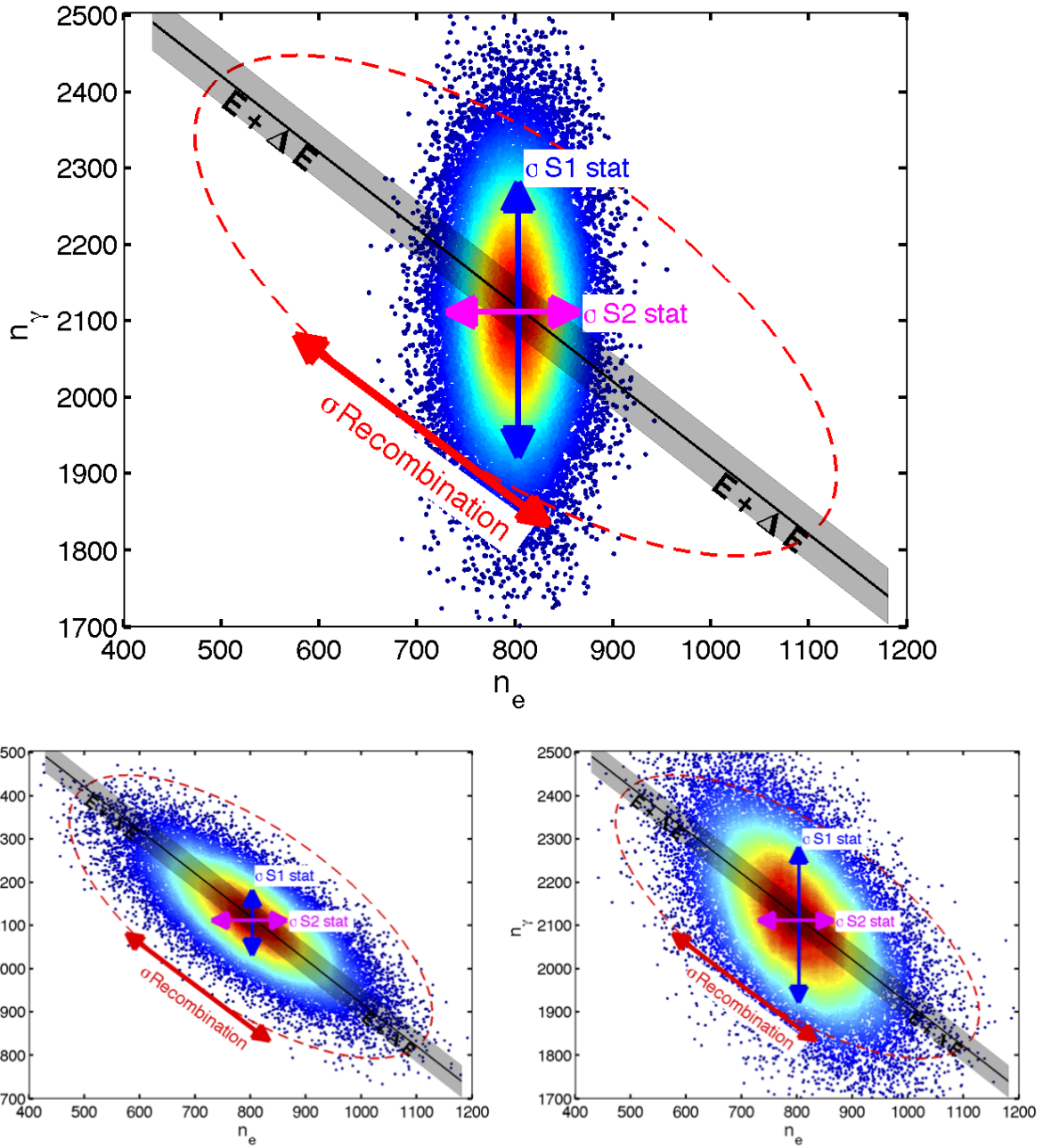


Figure 13: Top: Illustration of statistical variance, recombination fluctuations are set to 0. The spread in number of photons moves vertically and the spread in number of electrons moves horizontally. In black, a line of constant energy along the mean of combined energy with a width ΔE . Bottom left: Dominated by recombination fluctuations which move 45° to statistical variances. Bottom Right: Typical values for recombination and S1, S2 Stat for Kr^{83} .

The variable χ is used to represent the observed σ when dealing in bins of combined energy. Let's briefly consider the implication of equation 24. For the case of $\sigma_{n_{e\text{Det}}}^2 = \sigma_{n_{\gamma\text{Det}}}^2$, $M=0.5$, resulting in $\sigma_{n_{e\text{Det}}}^2 = \sigma_{n_{\gamma\text{Det}}}^2 = \chi_{\text{Det}}^2$. This case can be thought of as sweeping out equal variance from the statistical population which would for a circle as illustrated in Figure 13. For the case of $\sigma_{n_{e\text{Det}}}^2 \neq \sigma_{n_{\gamma\text{Det}}}^2$ the observed statistical variance in a slice of combined energy will become less than the variance of the best channel. Specifically for the LUX detector the implication of equation 24 is that the statistical variance measured in a slice of combined energy will collapse to less than that of the S2 statistical uncertainty, as bin width Δ_E goes to zero.

To complete the treatment of binned energy in this section we now add the final piece to the observed statistical variance, the contribution from the bin width Δ_E . The residual variance arises from rotating the population of 2D gaussian about the bin center, the rotation having a slope of M or $(1-M)$ as given in equation 23. Note, the residual term from the slope can also be removed by centroid subtraction of the photons and electrons vs. energy as discussed later in section 3.7, in that case we are only left with χ_{Det}^2 shared between the two channels.

$$\begin{aligned}\chi_{n_{\gamma\text{Det}}}^2 &= \chi_{\text{Det}}^2 + \frac{(MW\Delta_E)^2}{12} \\ \chi_{n_{e\text{Det}}}^2 &= \chi_{\text{Det}}^2 + \frac{((1-M)W\Delta_E)^2}{12}\end{aligned}\quad (25)$$

Were χ^2 is defined in 24, M is given in equation 23, W is the work function in [quanta/keV], Δ_E is a bin of energy [keV], the normalization of 12 arrises from the second moment of a rotated line about its center. The total observed variance, χ^2 , in the number of photons and electrons considering a bin of combined energy can now be determined transforming equation 17 to 26.

$$\begin{aligned}\chi_{n_\gamma}^2 &= \sigma_{n_{\text{ex}}}^2 + n_i F(r)^2 + \sigma_r^2 n_i^2 + \chi_{n_{\gamma\text{Det}}}^2 \\ \chi_{n_e}^2 &= n_i F(1-r)^2 + \sigma_r^2 n_i^2 + \chi_{n_{e\text{Det}}}^2\end{aligned}\quad (26)$$

In equation 26 we have defined the observed standard deviation in units of quanta χ for n_γ, n_e when working with bins of combined energy. In the limit that F , $\sigma_{n_{\text{ex}}}^2$ and Δ_E go to zero the observed variance in number of photons and electrons (χ_{n_γ} and χ_{n_e}) are related to the size of recombination fluctuations in a given combined energy bin, equation 27. Where σ_R is in units of quanta, $\sigma_R = n_i \sigma_r$.

$$\begin{aligned}\sigma_{R_\gamma}^2 &= \chi_{n_\gamma}^2 - \chi_{n_{\gamma\text{Det}}}^2 \\ \sigma_{R_e}^2 &= \chi_{n_e}^2 - \chi_{n_{e\text{Det}}}^2\end{aligned}\quad (27)$$

We have arrived at the conclusion of this section, armed with equation 27 we now have two methods for determining the size of recombination fluctuations, σ_R^2 where the subscript γ or e is used to represent the channel of quanta used for the calculation. Either the observed variance in the light and charge channel can be used to measure the size of recombination fluctuation in a bin of energy. Any asymmetry between the two methods has implications which are discussed in the following subsection.

3.4 Measuring the Fano Factor in Bins of Energy

There are three terms in equation 26 that give rise to an asymmetry between the observed variance $\sigma_{R_\gamma}^2$ and $\sigma_{R_e}^2$. The small difference in variance from the slope can be solved for exactly leaving just the Fano factor F and $\sigma_{n_{ex}}^2$. By taking the difference of variance in the two channels component of recombination variance drops out leaving only the Fano factor and the variance in number of exitons, given in equation 26.

$$\sigma_{R_\gamma}^2 - \sigma_{R_e}^2 = \sigma_{n_{ex}}^2 + n_i F(2r - 1) \quad (28)$$

F is the Fano factor, equation 15, $\sigma_{n_{ex}}^2$ is the variance of the number of exitons produced and r is the recombination fraction, equation 16. Consider the case such that variance in the number of exitons $\sigma_{n_{ex}}^2$ is much less than the contribution from the Fano factor. In such a regime we can solve for the Fano factor, potentially energy dependent, from equations 28.

$$F(E) = \frac{\sigma_{R_\gamma}^2 - \sigma_{R_e}^2}{n_i(2r - 1)} \left\{ r \neq \frac{1}{2} \right. \quad (29)$$

There is an underlying subtlety to equation 29. Remarkably, in the limit that Δ_E goes to zero the Fano factor can be extracted with minimal knowledge of intrinsic detector statistical variance. Further, when the statistical variance of S1 and S2 are identical the value of M (equation ??) will be 0.5. In that special case no knowledge of the statistical variance is needed to measure the Fano factor.

When $r = \frac{1}{2}$ the coefficient in front of the Fano factor becomes zero in equation 28. At this value an equal contribution from the Fano factor goes into the variance χ^2 of photons and electrons, allowing for the smaller value of σ_{ex}^2 to be extracted.

$$\sigma_{n_{ex}}^2 = \sigma_{R_\gamma}^2 - \sigma_{R_e}^2 \left\{ r = \frac{1}{2} \mid \sigma_{n_{ex}}^2 \gg n_i F(2r - 1) \right. \quad (30)$$

Equation 30 is also valid in the case that $\sigma_{n_{ex}}^2$ is much larger than the contribution form the Fano factor. This happens to be true when dealing with the time dependent light yield of ^{83m}Kr , this topic will be explored in the next section.

3.5 Application to ^{83}Kr

Using the high stats Kr83 calibration data we can validate the method for working in a bin of energy since the exact solution for recombination and detector fluctuations can be measured,

as outlined in section 3.1 and 3.3. Once the fluctuations from detector resolution are measured in the light and charge channel (S1 and S2 signals), the asymmetry between the two channels can be used to calculate the Fano factor (equation 26). The asymmetry in fluctuations in the light and charge channel arises from the Fano factor acting on ion production which is later amplified through the recombination fraction, as long as the recombination fraction does not equal 0.5. For the case of the ^{83m}Kr calibration the recombination fraction was 0.772 resulting in recombination fluctuations of 3 to 4 more quanta in the light channel as compared to the charge channel, see table 4. Though the additional recombination fluctuation is small having ample statistics the Fano factor can be constrained. The errors in the measurement were derived from simulated Kr data sets of 400,000 events with the Fano factor turned off, using 100 trials. First, recombination fluctuations were turned off and only fluctuations from detector resolution as calculated in section 3.1 were used, see Table 2. It was found that the error of the difference in recombination fluctuation from the light and charge channel ($\sigma_{R_\gamma}^2$ and $\sigma_{R_e}^2$) along with the error in ion production and recombination fraction were enough to constrain the Fano factor to 0.001-0.003. Next, the value of recombination was set slightly higher than the actual value of 82 to 100 quanta and the trials were repeated, see table 3. With the addition of recombination fluctuations to detector resolution fluctuations the error on measuring the Fano factor grew to 0.002-0.009, with smaller bin sizes (ΔE around the center leading to the smallest error as seen from equation 25).

ΔE [keV]	Count	$\sigma(\sigma_{R_\gamma}^2)$	$\sigma(\sigma_{R_e}^2)$	$\sigma(\sigma_{R_\gamma}^2 - \sigma_{R_e}^2)$	σF
0.025	1528	77.8	77.9	1.3	0.0008
0.05	3063	54.4	54.6	1.8	0.0012
0.1	6128	36.4	36.6	2.6	0.0016
0.2	12242	23.7	23.8	3.7	0.0023
0.25	15290	22.9	22.9	4.0	0.0026
0.5	30528	17.5	17.5	5.2	0.0033

Table 2: Values for the standard deviation of the observed value of σ_R^2 from n_γ and n_e along with the standard deviation of the difference, for a simulated ^{83m}Kr decay with recombination set to zero. Note, since the two methods for determining σ_R^2 are correlated the standard deviation of the measured difference is small leading to an improved error when calculating the Fano factor or $\sigma_{n_{ex}}^2$.

The results of the high stats calibration data are shown in table 4, containing 400k events in the fiducial volume of the detector. Using equation 27 we find good agreement between the method described in equation 18 and the recombination fluctuation calculated from the charge channel (σ_{R_γ} and σ_{R_e}). The accuracy helps us build confidence that the statistical components of the detector are modeled well enough to measure recombination fluctuation to within 3%. Further, the ability to see the asymmetry in recombination fluctuations between the light and charge channel demonstrates the power of using binned combined energy (section 3.3). Any observed difference between the two channels can only be from either the Fano factor or spread in exiton production, but we assume the fluctuations in exiton production are much less than fluctuations in ion production. The Fano factor is derived from equations 29 and the uncertainty was determined from simulations. The total fluctuation as

Δ_E [keV]	Count	$\sigma(\sigma_{R_\gamma}^2)$	$\sigma(\sigma_{R_e}^2)$	$\sigma(\sigma_{R_\gamma}^2 - \sigma_{R_e}^2)$	σF
0.025	1523	498	498	3.2	0.0020
0.05	3056	347	347	4.1	0.0026
0.1	6118	237	237	5.3	0.0033
0.2	12225	171	171	8.6	0.0054
0.25	15285	149	148	9.5	0.0060
0.5	30514	101	99.4	14.3	0.0090

Table 3: Values for the standard deviation of the observed value of σ_R^2 from n_γ and n_e along with the standard deviation of the difference, for a simulated ^{83m}Kr decay with recombination set to 100 quanta. Note, since the two methods for determining σ_R^2 are correlated the standard deviation of the measured difference is small leading to an improved error when calculating the Fano factor or $\sigma_{n_{ex}}^2$.

number of quanta is listed in the rightmost column. The Fano factor manifests itself as an asymmetry between fluctuations in the light and charge channel as given in equation 26, the recombination fraction was found to be $r = 0.772$ and the average number of ions produced per decay was $n_i = 2900$. Having demonstrated the method for a mono energetic calibration source the next step will be to apply the method on the continuous beta spectrum of the tritium data.

σ_R 18 (Quanta)	Δ_E (keV)	Count	$\sigma_{R_\gamma} = \sqrt{\chi_{n_\gamma}^2 - \chi_{n_{\gamma_{Det}}}^2}$ (Quanta)	$\sigma_{R_e} = \sqrt{\chi_{n_e}^2 - \chi_{n_{e_{Det}}}^2}$ (Quanta)	$F = \frac{\sigma_{R_\gamma}^2 - \sigma_{R_e}^2}{n_i(2r-1)}$ (Quanta)	$\sqrt{Fn_i}$ (Quanta)
82.4 ± 4.0	0.025	1518	87.2 ± 2.9	87.1 ± 2.9	0.010 ± 0.002	5.8 ± 0.5
	0.05	3124	85.0 ± 2.0	84.9 ± 2.0	0.005 ± 0.003	3.8 ± 1.1
	0.1	6269	87.8 ± 1.3	87.6 ± 1.3	0.023 ± 0.003	8.1 ± 0.5
	0.2	12508	90.0 ± 1.0	89.7 ± 1.0	0.021 ± 0.005	7.8 ± 0.9
	0.25	15557	88.5 ± 0.8	88.3 ± 0.8	0.013 ± 0.006	6.1 ± 1.3
	0.5	30826	87.0 ± 0.6	86.7 ± 0.6	0.027 ± 0.009	8.8 ± 2.2

Table 4: Values for the standard deviation of the observed value of σ_R^2 from n_γ and n_e along with the standard deviation of the difference, for a ^{83m}Kr data set with 400k events in the fiducial volume. The Fano factor is derived from equations 29 and the uncertainty was determined from simulations. The total fluctuation as number of quanta is listed in the rightmost column. The Fano factor manifests itself as an asymmetry between fluctuations in the light and charge channel as given in equation 26, with a recombination fraction of 0.772 and $n_i = 2900$.

3.6 Application to Tritium Data (any continuos spectrum)

Adapting the equation of the previous section to continuous energy spectra requires that the centriod of a continuos spectrum be subtracted off so that the variance from the light yield or charge yield vs. energy is removed. ...

After applying the Smearing Model of Section 4 we apply the method described in this section to extract recombination fluctuations form the tritium data.

In this subsection we test method outlined in section 3.3 for dealing in bins of combined energy specifically applied to the tritium beta spectrum, but the method outlined can be used for any continue spectrum. To first order the treatment of the continuous spectrum is identical to that outlined for the mono energetic source as outlined previously in subsection 3.3. Figure 14 illustrates a tritium beta spectrum convolved with detector resolution similar to that measured for the LUX detector, the figure is analogous to Figure 13. As the bin size around a value of combined energy is squeezed to zero the statistical variance in the number of photons and electrons converge, the value is given by equation 25. Whereas, regardless of bin size recombination fluctuations remain since they move along lines of constant energy. In order to adapt the methodology developed for a mono energetic source to a continuous energy spectra requires that the centriod of the light and charge yield be subtracted off. The slope in the light and charge channels from the fundamental yield induce a further variance on top of χ_{Det} from the population in an energy bin being tilted as demonstrated in figure 15. For the purposes of this study, we find it sufficient to fit a quadratic form to the centroid of the entire population and subtract off the local slope from the measured variance. An analogous methods for centriod subtraction to extract recombination fluctuations are described in detail in [Patrick's Thesis].

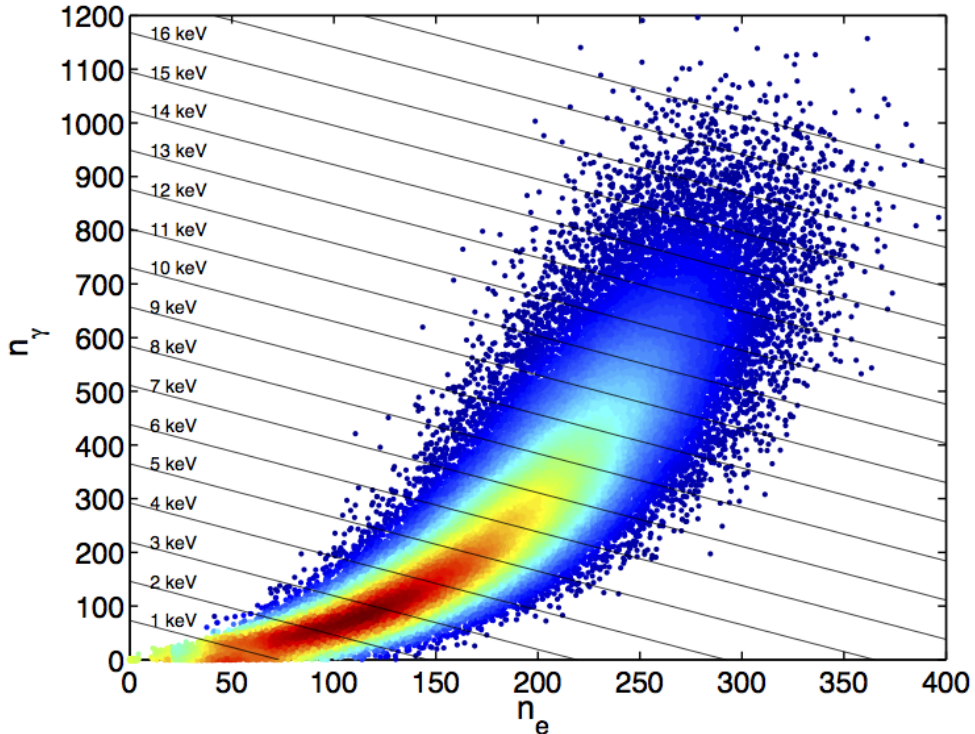


Figure 14: Illustration of statistical variance for the tritium beta spectrum, recombination fluctuations are set to 0. This plot is analogous to Figure 13 which illustrates the case for the mono energetic ^{83m}Kr decay. Recombination fluctuation move along lines of constant energy, S1 statistical fluctuation move vertically and S2 statistical fluctuations move horizontally.

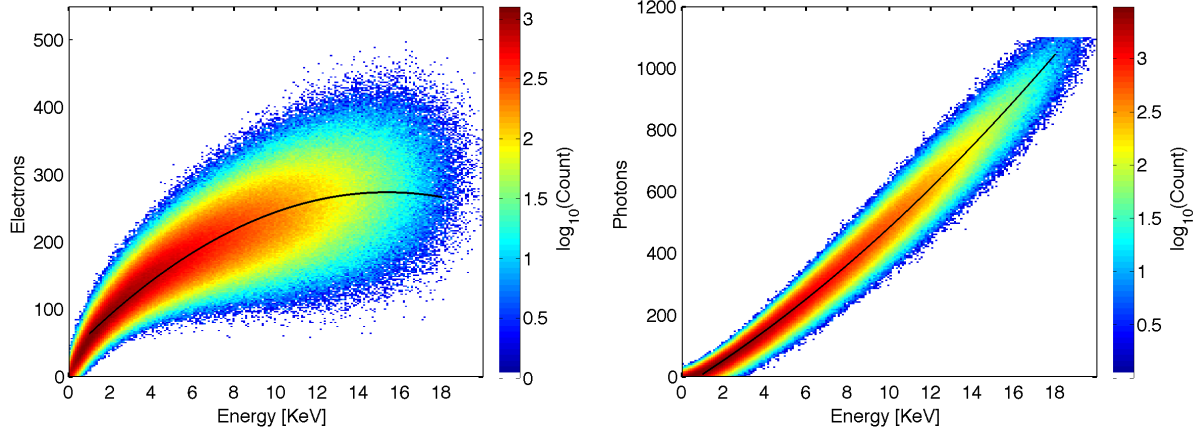


Figure 15: Illustration of statistical variance for the tritium beta spectrum, recombination fluctuations are set to 0. This plot is analogous to Figure 13 which illustrates the case for the mono energetic ^{83m}Kr decay. Recombination fluctuation move along lines of constant energy, S1 statistical fluctuation move vertically and S2 statistical fluctuations move horizontally.

3.7 Centriod Subtraction

For the case of a continuous source we expand upon the result from section 3.3 where the additional variance from detector resolution was calculated in an given energy bin as $\chi_{n_{\gamma}\text{Det}}^2$ and $\chi_{n_e\text{Det}}^2$. When dealing with a continuous source we must subtract off the centroid of the number of photons and electron vs. energy to remove additional variance induced by the slope. What results is a common variance from detector resolution shared by both the charge and light channel in each bin of energy, defined as $\chi_{\text{Det}}^2 = \chi_{n_{\gamma}\text{Det}}^2 = \chi_{n_e\text{Det}}^2$, equation 31. The result is deterred in 32 for a small variation in n_e around combined energy, and is identical to that derived for the case of the mono energetic source in equation 24 as the bin size ΔE goes to zero. Which is analogous to saying that the centroid subtraction removed the additional variance from the slope of light field and charge yield, which can be calculated to first order for a mono energetic source. And the slope of n_e with respect to $n_{\gamma} + n_e$ is $(1-M)$, given in 23. To demonstrate the method the measured detector resolution and a test recombination fluctuation input into a tritium simulation. The result is shown in figure 16 for various energy bin widths. We see that as long as the recombination is greater than χ_{Det} , which is being added in quadrature, the value of recombination can be determined to good precision using the method. The small deviation observed around the first and last bins is due to the spectral shape, a correction for spectral shape will be discussed in the next section and will improve the measurement of σ_R .

$$\begin{aligned}\sigma_{R_{\gamma}}^2 &= \chi_{n_{\gamma}}^2 - \chi_{n_{\text{Det}}}^2 \\ \sigma_{R_e}^2 &= \chi_{n_e}^2 - \chi_{e_{\text{Det}}}^2\end{aligned}\tag{31}$$

$$\begin{aligned}
\delta[\Delta n_e] &= \delta[n_e] - \delta \left[\langle n_e \rangle_{n_e+n_\gamma} \right] \\
&= \cancel{\frac{dn_e}{dn_e}}^1 \delta[n_e] + \cancel{\frac{dn_e}{dn_\gamma}}^0 \delta[n_\gamma] - \delta \left[\langle n_e \rangle_{n_e+n_\gamma} \right] \\
&= \delta[n_e] - \frac{d \langle n_e \rangle}{d(n_e + n_\gamma)} \frac{d(n_e + n_\gamma)}{dn_e} \delta[n_e] - \frac{d \langle n_e \rangle}{d(n_e + n_\gamma)} \frac{d(n_e + n_\gamma)}{dn_\gamma} \delta[n_\gamma] \\
\delta[\Delta n_e] &= \delta[n_e] - (\delta[n_\gamma] + \delta[n_e]) \frac{d \langle n_e + n_\gamma \rangle}{d(n_e + n_\gamma)} \\
\delta[\Delta n_e] &= (M)\delta[n_e] - (1-M)\delta[n_\gamma] \\
\chi^2_{Det} &= Var(\Delta n_e) = (M)^2 \delta^2[n_e] + (1-M)^2 \delta^2[n_\gamma] - 2M(1-M) \cancel{\delta[n_e]\delta[n_\gamma]}^0
\end{aligned} \tag{32}$$

The tritium spectral shape may cause a perturbation to the analytic solution for observed variance χ^2 , equation 25. To observe any discrepancy we test the analytic solution against the observed variance of a simulated tritium spectrum. Figure 16 shows the result of the analytic solution vs. the observed variance in several bin widths. The analytic solution is sufficient to first order, we ignore second order corrections in this analysis. [add table showing the tiny difference in variance]. After correcting observables for the tritium beta spectral shape (discussed in Section 4) we will be ready to use the tools of this section to decouple detector resolution and measure recombination fluctuations from the tritium data

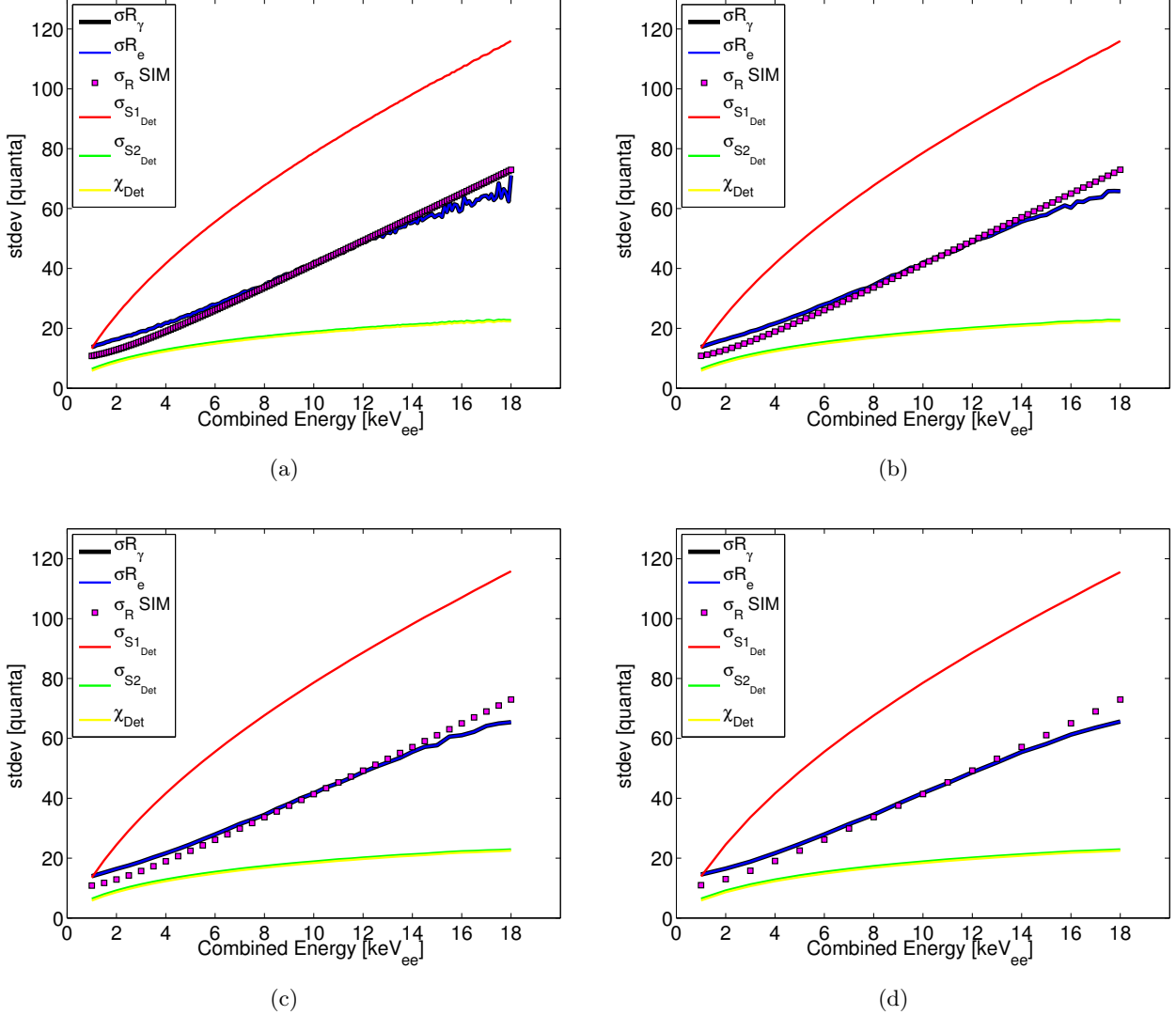


Figure 16: Simulated tritium spectrum with the detector resolution of the LUX detector, $\sigma_{S1_{\text{Det}}}$ and $\sigma_{S2_{\text{Det}}}$, and an arbitrary recombination fluctuation σR (magenta). After centroid subtraction we apply the methodology described in the previous section to extract σR (black and blue) through the light and charge channel using our knowledge of detector resolution per each energy bin χ_{Det} (green), $S1_{\text{Det}}$ (red) and $S2_{\text{Det}}$ (yellow). The plots show cases for various bin widths in [KeV]: a) $\Delta E = 0.1$ b) $\Delta E = 0.25$ c) $\Delta E = 0.5$ d) $\Delta E = 1$.

4 Correcting the Tritium Spectral Shape for Finite Resolution

The goal of the following two sections is to extract light yield, charge yield and recombination fluctuations from the tritium spectrum using the methods described in section 3.3. The first step is to use the NEST model in an attempt to undue the effect of the tritium spectral shape and finite detector resolution, described in this section. We find that the light yield and charge yields extracted from the data deviate too much to apply the correction factor.

Since the correction is found to be small we can proceed to extract new LY, QY and σR from the tritium data without correction building a model that better reproduces the data than the NEST model (which has yet to be vetted at our electric field and energy). We then take that improved model and apply the correction.

The distribution of tritium events convolved with the detector's finite resolution for S1 (scintillation) and S2 (ionization) causes the observed mean to shift from the actual mean. The shift is non trivial and depends on the spectral shape and the functional form resolution over a range of energies. A large negative derivative of the spectral shape will tend to pull the observed spectrum to lower values, and the functional form of the resolution will also shift the spectrum. Figure 17 and equations 34,37 demonstrate a simple model to solve for the relation between observed mean and actual mean. Take for example a linearly declining distribution, starting with infinite detector resolution we set up bins of width Δx . To account for finite energy resolution we distribute the counts in each rectangular bin into Gaussians centered at μ_i , with a spread of σ_i , and normalized to the area of the bin $N_i \times \Delta x$ with amplitude c_i . Each rectangular bin(i) can be written as a Gaussian $G(i)$:

$$c_i = \frac{N_i \times \Delta x}{\sigma_i \sqrt{2\pi}}$$

$$G_i(x) = c_i \times \exp\left(\frac{-(x - \mu_i)^2}{2\sigma_i^2}\right)$$
(33)

Where N_i is the count in the i^{th} bin, Δx is the bin width, μ_i is the bin center and σ_i is the resolution at the i^{th} bin. Figure 17 show the application of equation 33 to a linear energy distribution with a \sqrt{E} dependent σ . The observed distribution is the sum of the Gaussians, shown in red.

4.1 Calculating the Observed Energy

After modeling the finite resolution with Gaussians the mean observed at each bin can be calculated from the overlap of all bins weighted by the corresponding means. We can write the observed mean in the i^{th} bin, ν_i , in terms of the bin centers μ and overlapping areas of

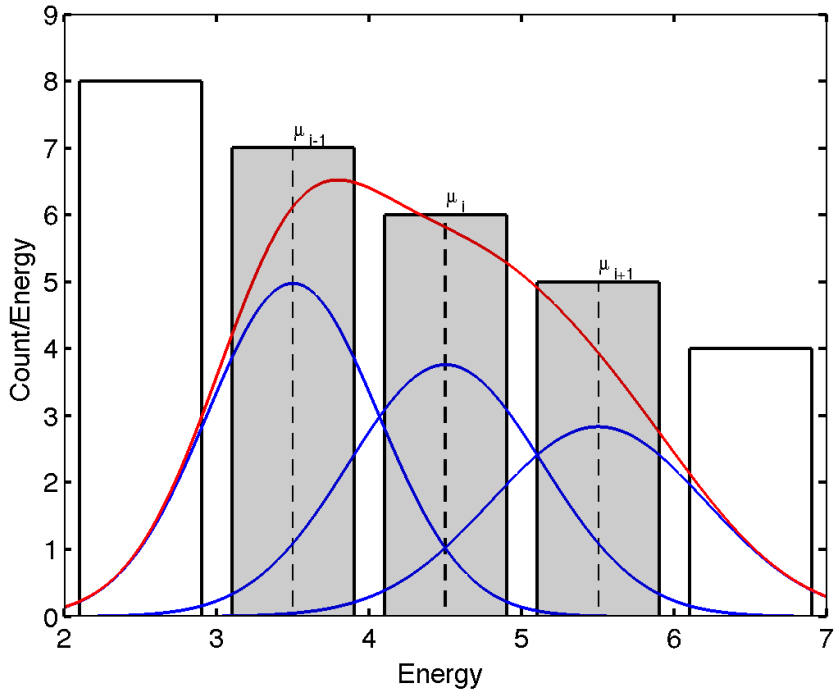


Figure 17

all bins using equation 33:

$$\nu_i = \frac{\sum_{j=1}^n \mu_j \int_{\mu_i - \frac{\Delta x}{2}}^{\mu_i + \frac{\Delta x}{2}} G_j(x) dx}{\sum_{j=1}^n \int_{\mu_i - \frac{\Delta x}{2}}^{\mu_i + \frac{\Delta x}{2}} G_j(x) dx} \quad (34)$$

Equation 34 can be solved in terms of error function and complimentary error function, first we will generalize a formula to solve for the overlapping area from the j^{th} bin into the i^{th} bin.

$$A_{i,j} = \int_{\mu_i - \frac{\Delta x}{2}}^{\mu_i + \frac{\Delta x}{2}} G_j(x) dx = \begin{cases} c_i \operatorname{erf} \left(\frac{\Delta x}{\sigma_i \sqrt{2}} \right), & j = i \\ \frac{c_j}{2} \operatorname{erfc} \left(\frac{|\mu_j - \mu_i| - \frac{\Delta x}{2}}{\sigma_j \sqrt{2}} \right) - \frac{c_j}{2} \operatorname{erfc} \left(\frac{|\mu_j - \mu_i| + \frac{\Delta x}{2}}{\sigma_j \sqrt{2}} \right), & j \neq i \end{cases} \quad (35)$$

As μ approaches zero the Gaussian distribution of equation 33 begins to spill over into negative values, which in some cases may be unphysical. For instance, the Gaussian assumption leads to negative photons. We can chose to ignore this area or make the distribution more Poisson like by bouncing the Gaussian back at $\mu = 0$. The formula for accounting for the area of the reflected Gaussian is described in 36. Ultimately this assumption has little impact on the S1 and S2 analysis because the threshold cut off well before the zero interface is reached, but it does make the distributions more Poisson like near the zeroth bins. Equation 36 is the same as 35 with the bin center μ_i mapped to $-\mu_i$.

$$B_{i,j} = \frac{c_j}{2} \operatorname{erfc} \left(\frac{|\mu_j + \mu_i| - \frac{\Delta x}{2}}{\sigma_j \sqrt{2}} \right) - \frac{c_j}{2} \operatorname{erfc} \left(\frac{|\mu_j + \mu_i| + \frac{\Delta x}{2}}{\sigma_j \sqrt{2}} \right) \quad (36)$$

The error function and complementary error function are defined in equation 37 and the coefficient c_i is defined in equation 33.

$$\begin{aligned} \operatorname{erf}(x) &= \frac{2}{\sqrt{\pi}} \times \int_0^x \exp(-t^2) \\ \operatorname{erfc}(x) &= \frac{2}{\sqrt{\pi}} \times \int_x^\infty \exp(-t^2) = 1 - \operatorname{erf}(x) \end{aligned} \quad (37)$$

Finally, we solve for the observed mean in the i^{th} bin by summing all the Gaussian overlaps $A_{i,j} + B_{i,j}$ (equations 35,36), weighting the overlapping area from each bin by the corresponding bin center μ_j . The result is shown in equation 38 and is equivalent to equation 34 when the area from the reflected Gaussian is not considered, $B_{i,j}=0$.

$$\nu_i = \frac{\sum_{j=1}^n \mu_j \cdot (A_{i,j} + B_{i,j})}{\sum_{j=1}^n (A_{i,j} + B_{i,j})} \quad (38)$$

4.2 Smearing a Toy Spectrum

To demonstrate the application of equation 38 we use it to smear a toy linearly decaying spectrum. By modifying the dependence of σ_i on μ_i we can better understand the effects of the spectral shape and the functional for of the resolution.

Figure 18 shows the effect of the finite resolution on a linearly decaying spectral shape. Using a constant resolution σ the observed mean, when accounting for finite resolution, shifts down due to the spectral shape. In the case with $\sigma_i \sim \sqrt{\mu_i}$ the observed mean at first

shifts higher as the increasing width at higher value bin centers, even with lower counts, out weighs the lower bin centers with higher counts and narrower widths. In both cases as the bin centers approach zero the observed mean shifts higher due to an imposed threshold at zero, here Poisson statistics take over and the Gaussian characterization leads to a loss of events below zero. Thus, for the sake of the toy model in figure 18 we only characterize the relation between the real mean and the observed mean from the second bin center.

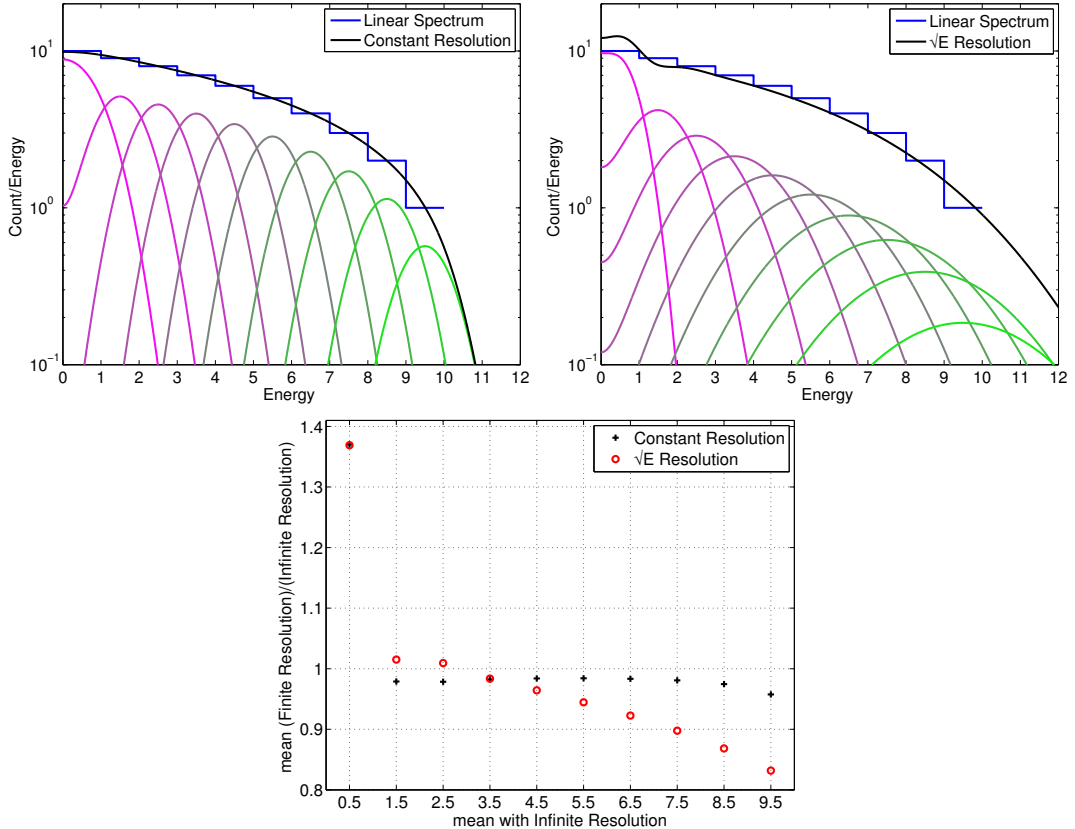


Figure 18: Top Left: A linearly decaying spectrum, in blue. The black curve represents the sum of the Gaussians assuming a constant resolution. Top Right: A linearly decaying spectrum, in blue. The black curve represents the sum of the Gaussians with a \sqrt{E} dependent resolution. Bottom: The observed mean, with finite resolution, compared to the real mean with infinite resolution. The black points are for the case with linear resolution and the red points represent the case with \sqrt{E} dependent resolution.

5 Measuring LQ, QY and Recombination, Uncorrected for Spectral shape

5.1 Tritium S1 Mean and NEST

The correction for the mean of the measured light yield, S1 [Phe], for tritium beta decay can be solved for using equation 38. Starting with a simulated S1 tritium spectrum with infinite resolution and applying equations 33-38 one can attain the mapping of measured mean to true mean. The resolution of S1 was determined from statistical and instrumental fluctuations and is given in equation 12 and 13. The use of Gaussian error down to low S1 is an acceptable approximation since underlying distribution actually consists of the number of photons, $n_\gamma = \frac{S_1}{g_1}$. With $g_1=0.097$ there are still 20 photons near the S1 threshold of 2 [Phe], thus the Gaussian model is still a close approximation of the underlying Poisson distribution. We will use the Gaussian approximation as it makes the application of equations 33-38 much simpler. The variance in S1 is the result of recombination fluctuations, statistical fluctuations and instrumental fluctuations at a given energy. The functional form of all three have been previously measured and can be extrapolated for use with the tritium spectrum. The first step is to use the expected light yields from NEST along with the measured smearing from recombination and detector resolution to extract a correction factor for the observed S1 signal. Having a priori knowledge of light yields will allow for the spectral shape to be corrected or can at least be used to approximate an error when we go to extract the light yield and recombination fluctuations from the tritium beta spectrum.

$$\sigma_{S1}^2 = g_1^2(\sigma_{n_{\gamma,\text{stat}}}^2 + \sigma_{n_{\gamma,\text{inst}}}^2 + \sigma_R^2) \quad (39)$$

Figure 19 shows the application of smearing from equation 39 applied to the expected S1 tritium spectrum from NEST overlaid with the data. The mapping for converting the observed S1 to the real S1 is shown in figure 19. To calculate the correction we start with the NEST light yield, apply the measured g_1 , convolve it with a tritium beta spectrum and add in our first approximation of recombination fluctuations measured in equation 22, given infinite detector resolution this is the spectrum the LUX detector would observe in S1 space. Having calculated the dependence of detector resolution vs. the number of photons of a given event (equation ??) we can apply the smearing as outlined in 4 and calculate the shift from observed mean photons to real mean photons.

5.2 Tritium S2 Mean and NEST

The correction for the mean of the measured charge yield, S2 [Phe], for tritium beta decay can be solved for using equation 38. Starting with a simulated S2 tritium spectrum with infinite resolution and applying equations 33-38 one can attain the mapping of measured mean to true mean. The resolution of S2 was determined from statistical and instrumental fluctuations and is given in equation 12 and 13. The use of Gaussian error down to low S2 is an acceptable approximation since the S2 spectrum ends at 300 [Phe], $n_e = \frac{S_2}{g_2}$. With $g_2=5.75$ there are still 50 electrons near end of the tritium spectrum, thus the Gaussian

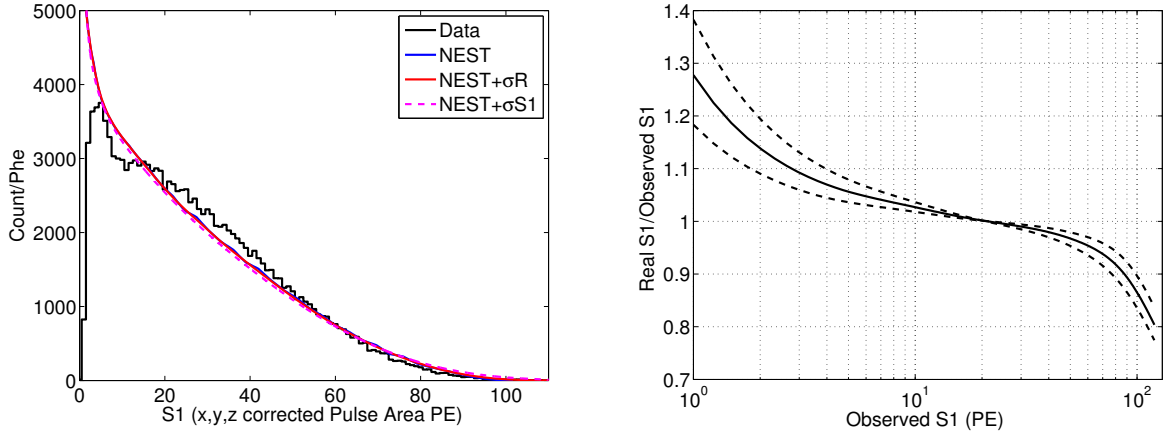


Figure 19: Top: In Black, a simulated tritium photon spectrum. In red, the mean of the spectrum after applying finite energy resolution of equation 38. Bottom Left: Mapping of the observed mean, with finite resolution, to the mean with infinite resolution for a tritium photon spectrum. Bottom Right: The ratio of the real mean to the observed mean vs. the observed mean for a tritium photon spectrum. Note the S1 threshold at about 2 Phe in S1.

model is still a close approximation of the underlying Poisson distribution. We will use the Gaussian approximation as it makes the application of equations 33–38 much simpler. As in the case of the light yield, the variance in S2 is the result of recombination fluctuations, statistical fluctuations and instrumental fluctuations at a given energy. The functional form of all three have been previously measured and can be extrapolated for use with the tritium spectrum. We first use the expected charge yields from NEST along with the measured smearing from recombination and detector resolution to extract a correction factor for the observed S2 signal. Having a priori knowledge of light yields will allow for the spectral shape to be corrected or can at least be used to approximate an error when we go to extract the charge yield and recombination fluctuations from the tritium beta spectrum.

$$\sigma_{S2}^2 = g_2^2(\sigma_{n_{e\text{stat}}}^2 + \sigma_{n_{e\text{inst}}}^2 + \sigma_R^2) \quad (40)$$

Figure 20 shows the application of smearing from equation 40 applied to the S2 tritium spectrum expected from NEST overlaid with the data. As with the S1 spectrum the correction is calculated using NEST for charge yield with the measured g_2 applied, convolve it with a tritium beta spectrum and using our first approximation of recombination fluctuations measured in equation 22, given infinite detector resolution this is the spectrum the LUX detector would observe in S2 space. Having calculated the dependence of detector resolution vs. the number of photons of a given event (equation ??) we can apply the smearing as outlined in 4 and calculate the shift from observed mean photons to real mean photons. From the S2 spectrum, which is more peaked than the S1, we see the 20% discrepancy with the NEST charge yield model but it may also be an indication of the error in g_1 and g_2 .

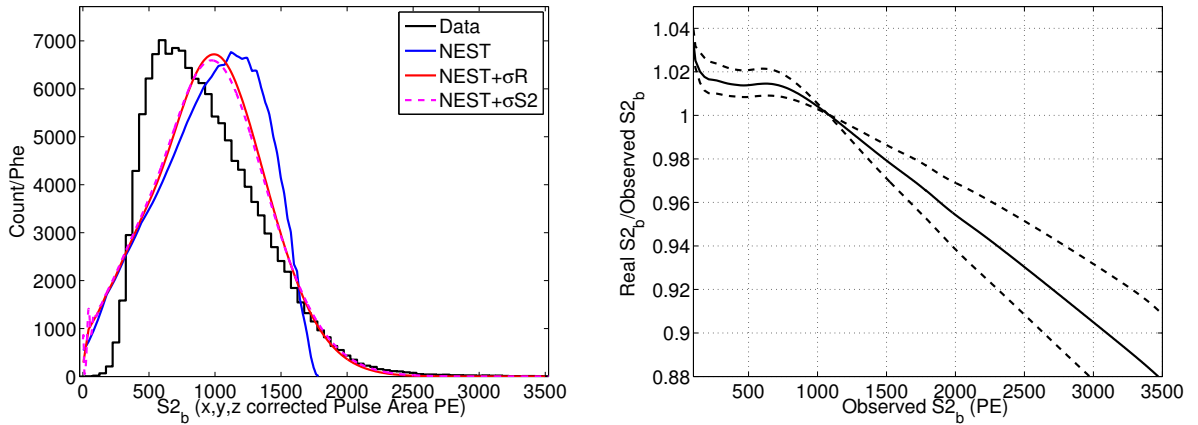


Figure 20: Top: In Black, a simulated tritium electron spectrum. In red, the mean of the spectrum after applying finite energy resolution of equation 38. Bottom Left: Mapping of the observed mean, with finite resolution, to the mean with infinite resolution for a tritium electron spectrum. Bottom Right: The ratio of the real mean to the observed mean vs. the observed mean for a tritium electron spectrum. Note the S2 threshold is around 500 Phe, due to the S1 threshold at 2 Phe.

5.3 Tritium Energy Spectrum

The mapping of the observed energy to real energy was determined using a full simulation of tritium beta decay. The accuracy of the smearing model described in equations 33-38 can be tested by comparing it against the energy observed after a full NEST simulation. The energy depends on both S1 and S2 thus, mapping observed energy to true energy may be non trivial. Again, we start with a simulated tritium energy spectrum with infinite resolution and apply the empirically determined resolution in equation 46, measured with ^{127}Xe X-rays and $^{83\text{m}}\text{Kr}$ calibrations. Figure 21 shows the comparison of smearing model vs true energy along with the smearing after running full photon and electron propagation in LUXSIM vs the true energy. The smearing form the model described in equations 33-38 is almost identical to the output of LUXSIM. The energy spectrum flares out at low energy, is pulled in from 5-10 [keV] and again flares out slightly above 15 [keV]. It is important to note that the change in the spectral shape is hardly noticeable, as was the case with S1 and somewhat with S2. Figure 22 shows the results for mapping observed energy to real energy using both smearing methods. The two methods show good agreement down to the threshold of 1.5 [keV], the agreement with simulation is always within 1%. Below 2 [keV] the model predicts the ratio of true energy to observed energy to rise as there are greater number of events at higher energy spilling over to lower energy, the simulation however does not show this behavior leading to a 5% discrepancy in the 1 [keV] bin. We take the difference between the smearing model and LUXSIM as a systematic uncertainty.

Using equation 29, 6 and 41 we solve for the spread in E as a function energy 46. a_γ and a_e are the coefficients in front of the root n term on the n_γ and n_e statistical variance . $W=73 \left[\frac{N_{\text{quanta}}}{\text{keV}} \right]$.

$$E = \frac{1}{W} (n_\gamma + n_{e^-}) \quad (41)$$

$$\sigma E^2 = \frac{1}{W^2} (\sigma n_\gamma^2 + \sigma n_{e^-}^2) \quad (42)$$

$$\sigma E^2 = \frac{1}{W^2} (a_\gamma^2 n_\gamma + a_{e^-}^2 n_{e^-}) \quad (43)$$

$$\sigma E^2 = \frac{(a_\gamma + a_{e^-})^2}{W} \frac{(n_\gamma + n_{e^-})}{W} \quad (44)$$

$$\sigma E^2 = \frac{(a_\gamma + a_{e^-})^2}{W} E \quad (45)$$

$$\sigma E = \frac{(a_\gamma + a_{e^-})}{\sqrt{W}} \sqrt{E} \quad (46)$$

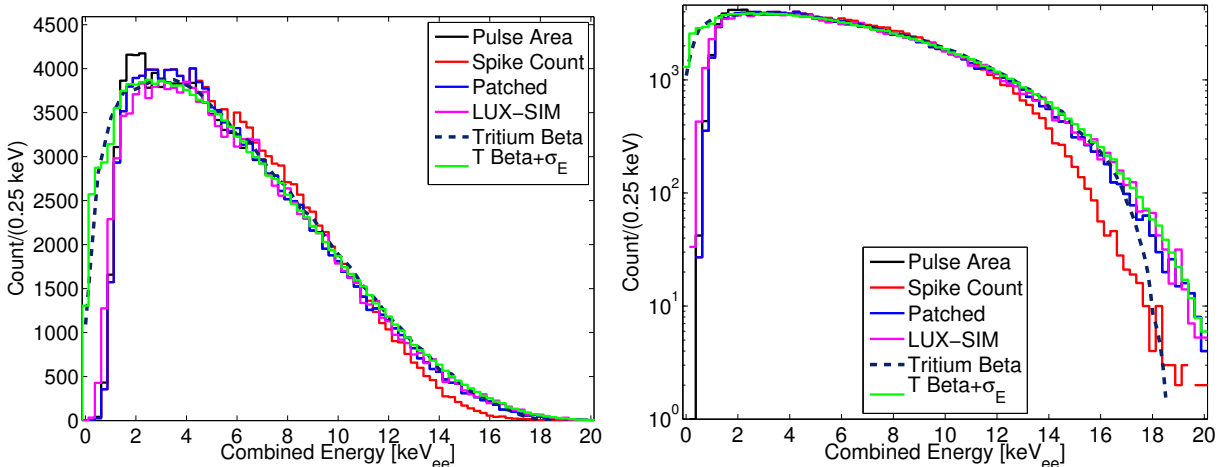


Figure 21: MC vs. Data, with detector threshold. And smeared MC vs all MC without a detector threshold.

5.4 LY, QY, σR Result

It is found that the S1 and S2 spectral shape is not a good match with the light yield model from NEST, thus applying a correction to the observed means using NEST is not prudent. Fortunately, we see that both in the S1 and S2 region of interest were the majority of the tritium events occur the spectral shape correction is less than 10%. Further, the reconstructed energy, uncorrected for spectral shape, is go to within 10% as well. Knowing this we can move forward with extracting a more accurate light yield and recombination fluctuation accepting the small error in order to create a more accurate model than NEST to which then we can apply the spectral shape correction.

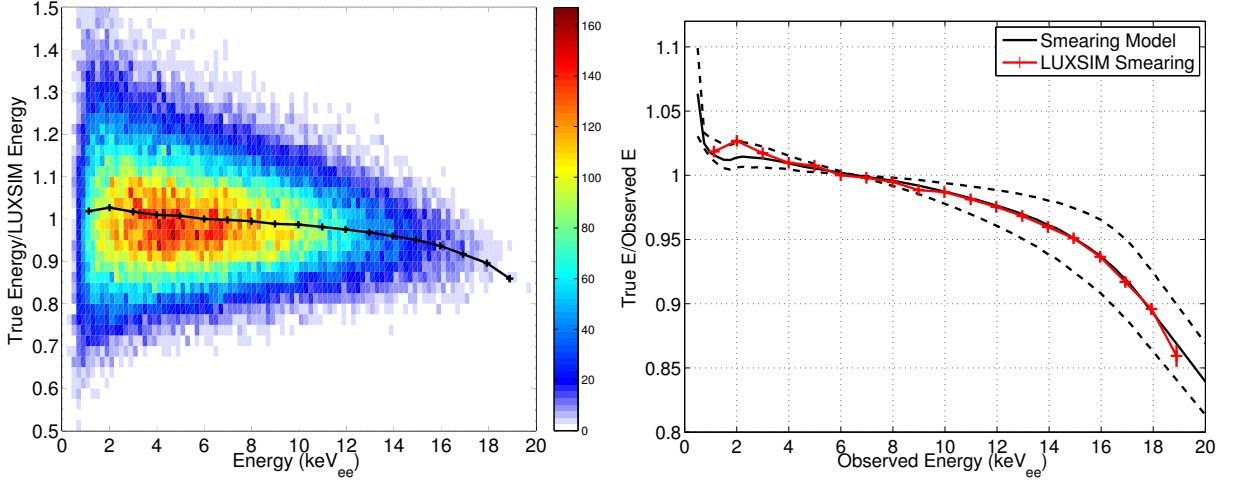


Figure 22: Left, mapping from real Monte Carlo energy to observed energy after applying a finite resolution using LUXSIM. Right, comparing the correction determined from the Monte Carlo (Red) to the detector smearing model (black) given in equation 46. The dashed lines represent the uncertainty in the measured value of $F(E)$. The agreement is within errors from 1 to 18 keVee. The Energy threshold is near 1.0 keVee.

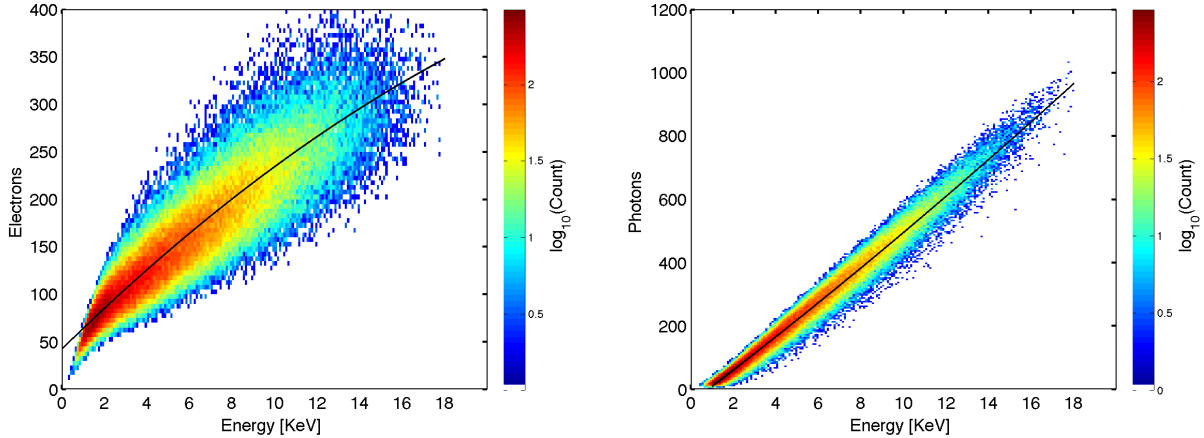


Figure 23: The data, assuming our g1g2

6 The Standard Candle. Light Yield from ^{83m}Kr

Quenching of scintillation yield vs. field has been typically defined relative to 32.1 keV decay of ^{83m}Kr at zero field [1],[2]. ^{83m}Kr first emits a 32.1 [keV] gamma followed by a 9.4 [keV] with a half life of 154 [ns] between the two (refs). The combined signal (41.6 [keV]) is found by the pulse finder in the majority of cases, using the standard WIMP search pulse gap setting of 500 ns. However, the combined signal is not useful as a standard calibration since the light yield from the second 9.4 keV decay depends strongly on decay time separation. The second 9.4 keV decay is effected by the presence of exitons from the initial 32.1 [keV]

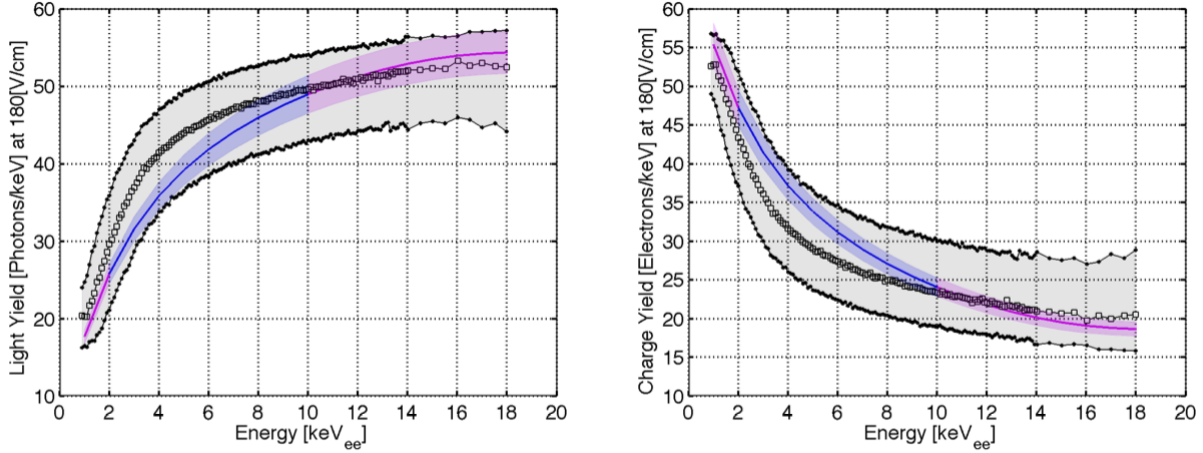


Figure 24: Light yield and charge yield from tritium data without spectral shape correction.

decay. See figure [show LUX result]

Fortunately, the first 32.1 keV appears to have no time dependance as it decays in ‘relaxed’ xenon without the presence of additional exitons [1]. For purposes of light yield normalization at zero field the 32.1 keV gamma serves as a good low energy standard candle for xenon detectors.

There were two data sets in late 2013 that contain ^{83m}Kr decays at zero field. Since the S2 (charge) signal is unavailable the top-bottom asymmetry, $\frac{\text{top-bottom}}{\text{top+bottom}}$, is used to define the Z coordinate for position dependent corrections. The XY correction is subdominant to the Z dependent correction for light yield. Figure [] shows the linear mapping from top-bottom asymmetry to detector depth (Z). With the Z correction applied the average pulse area (Phe) normalized to the detector center (241.6 mm below the gate grid) is found to be $267.4 \pm^{\text{stat}} 1.5 \pm^{\text{sys}} 5$. See Figure 26.

6.1 Field dependence of light yield from the 32.1 keV gamma of ^{83m}Kr

Charge separation increases with drift field leading to less recombination for light production, causing scintillation yield to be quenched. See table 5 for a list of the measured scintillation of the 32.1 keV gamma from ^{83m}Kr , also includes the NEST predictions.

Field [V/cm]	S1[Phe]	Photons[n $_{\gamma}$]	Yield [n $_{\gamma}$ /keV]	NEST [n $_{\gamma}$ /keV]
0	267.4 ± 6.5	1980 ± 40.7	61.7 ± 1.27	64.2 ± 2.6
51	246.7 ± 1.2	1827.4 ± 8.9	56.9 ± 0.28	60.8 ± 2.5
105	233.6 ± 1.4	1730.4 ± 10.4	53.9 ± 0.32	58.3 ± 2.3
182	212.3 ± 1.3	1572.6 ± 9.6	49.0 ± 0.30	54.9 ± 2.1

Table 5: Field dependance of the light yield form the 32.1 keV decay of ^{83m}Kr . The fields are calculated using a two dimensional model and not accounting potential charge accumulation on inner teflon panels.

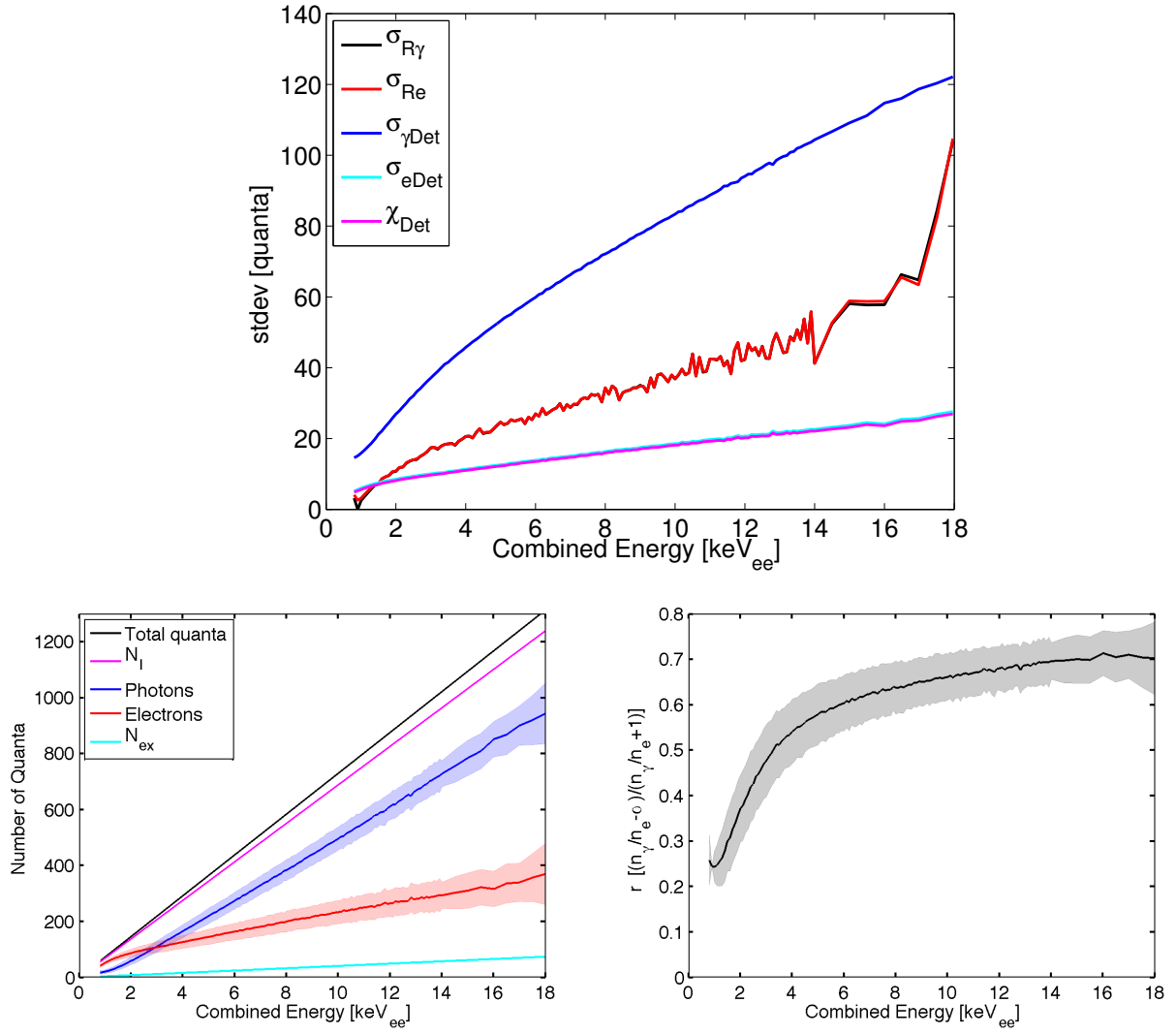


Figure 25: Extracting recombintion.

7 Scintillation Yield and Ionization Yield from Tritium Beta Decay

7.1 Cuts used in this analysis

- Standard LIX Pulse finder classifier used in the WIMP search.
- $S2_b > 100[\text{Phe}]$
- PDE (g1) = 0.138 ± 0.005 , measured with Tritium
- Extraction = 0.655 ± 0.02 measured with Tritium.

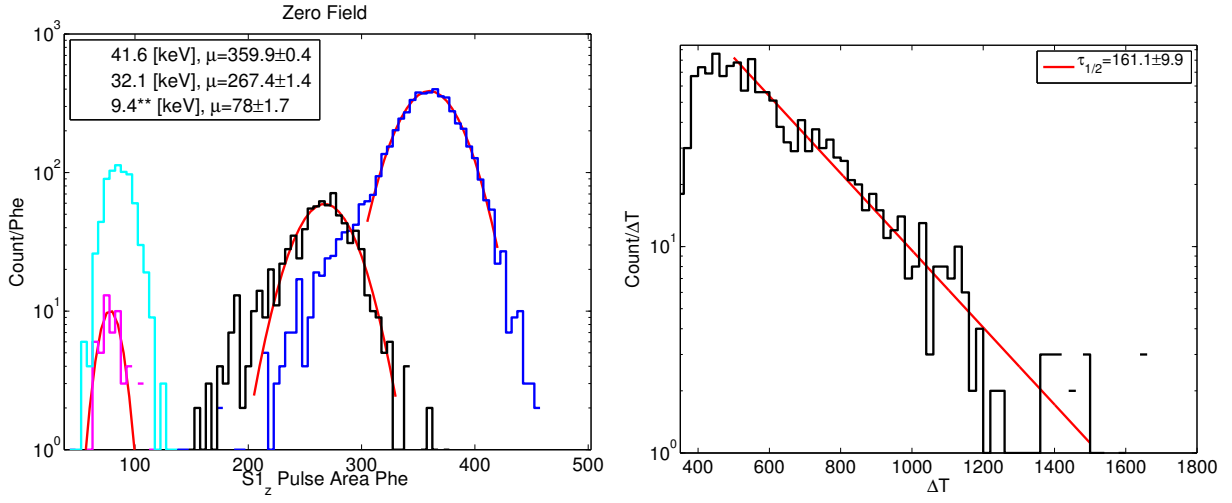


Figure 26: Left: ^{83m}Kr peaks at zero field. ** The 9.4 keV peak is fit only for events with a decay time separation greater than 1000 [ns]. Right: shows the timing separation between the 32.1 and 9.4 [keV] decays plotted above.

- single e- = 9.95 ± 0.1 [Phe/e-]
- Using NEST 4c bands.

7.2 Results at 180 [V/cm], Corrected for Spectral Shape

See Figures 27 and 28.

The scintillation and ionization yield is defined as [Photons/keV] and [Electrons/keV] respectively. For conversion of pulse area to photons and electrons along with the combined energy calculation see section 6. The measurement was made using a tritiated methane calibration source which provides betas ranging from > 1 to about 18 [keV]. Over 150,000 beta decay events, in the fiducial volume, were used to measure scintillation and ionization yield at 180 [V/cm]. Figure 27 shows the results from the tritium calibration before correcting for the shape of the tritium spectrum.

7.3 Results at 100 [V/cm], Corrected for Spectral Shape

... See Figure 29.

7.4 Compared With recent Compton Scattering Measurement

... See Figure 30.

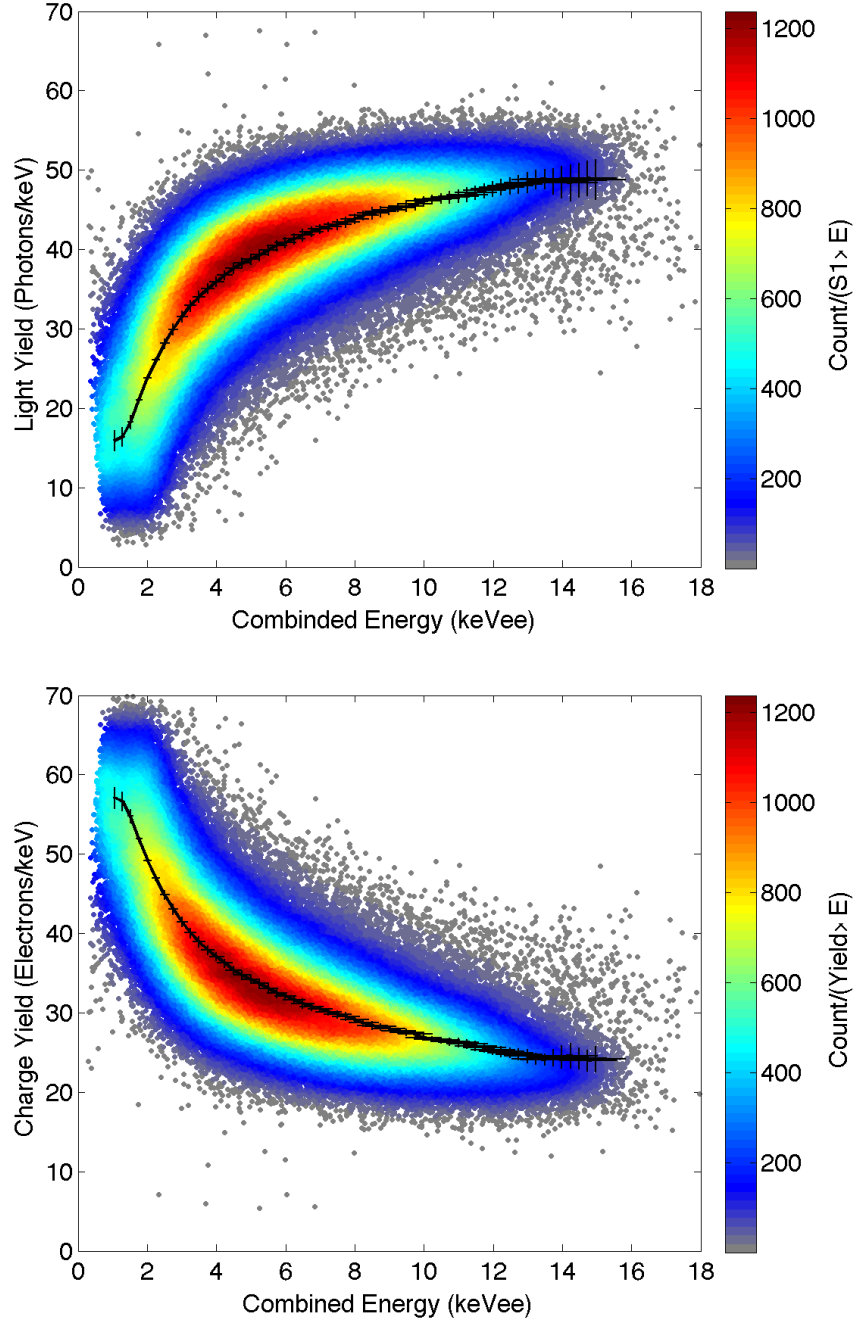


Figure 27: Top: Scintillation yield vs. combined energy using tritium beta decay. Bottom: Ionization yield vs. combined energy using tritium beta decay. At a drift field of 180 [V/cm], in the fiducial volume, and containing over 150,000 beta decays. The S1, S2 and energy has been corrected for spectral shape and detector resolution. The endpoint of the tritium beta spectrum is 18.6 [keV].

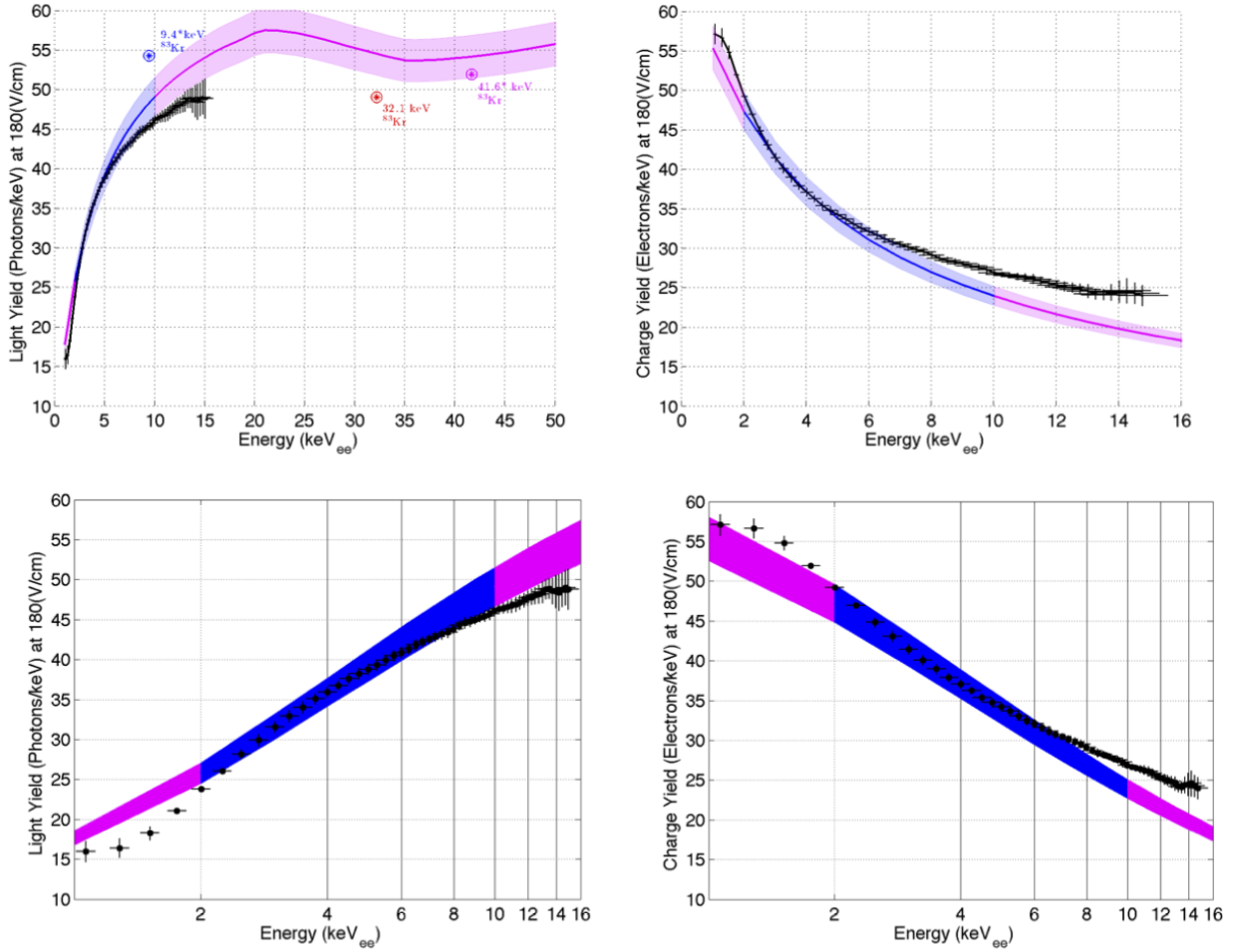


Figure 28: 180 [V/cm], corrected for spectral shape. Top Left: Mean scintillation yield vs. combined energy using tritium beta decay (black line). ⁸³Kr lines are plotted for reference but only the 32.1 [keV] line (red star) is kosher since the 9.4 [keV] line is dependent on timing separation, the 9.4 [keV] line is plotted (blue star) for separations greater than 1000 [ns]. Top Right: Mean ionization yield vs. combined energy (black line). Bottom Left: Scintillation yield vs. combined energy on a log scale. Bottom Right: Ionization yield vs. combined energy on a log scale. The shaded blue regions represent the NEST mean with $\pm 5\%$ that has been vetted by data [Erik Dahl Thesis]. The shaded magenta regions represent the NEST extrapolations from data. The measurement is made at a field of 180 [V/cm] and contains over 150,000 beta decays. The endpoint of the tritium beta spectrum is 18.6 [keV]

8 Fixing the Low Energy Tritium ‘Pile Up’

By modifying the scintillation yield down and ionization yield up at low energy the strange ‘pile up’ at low energies can be resolved.

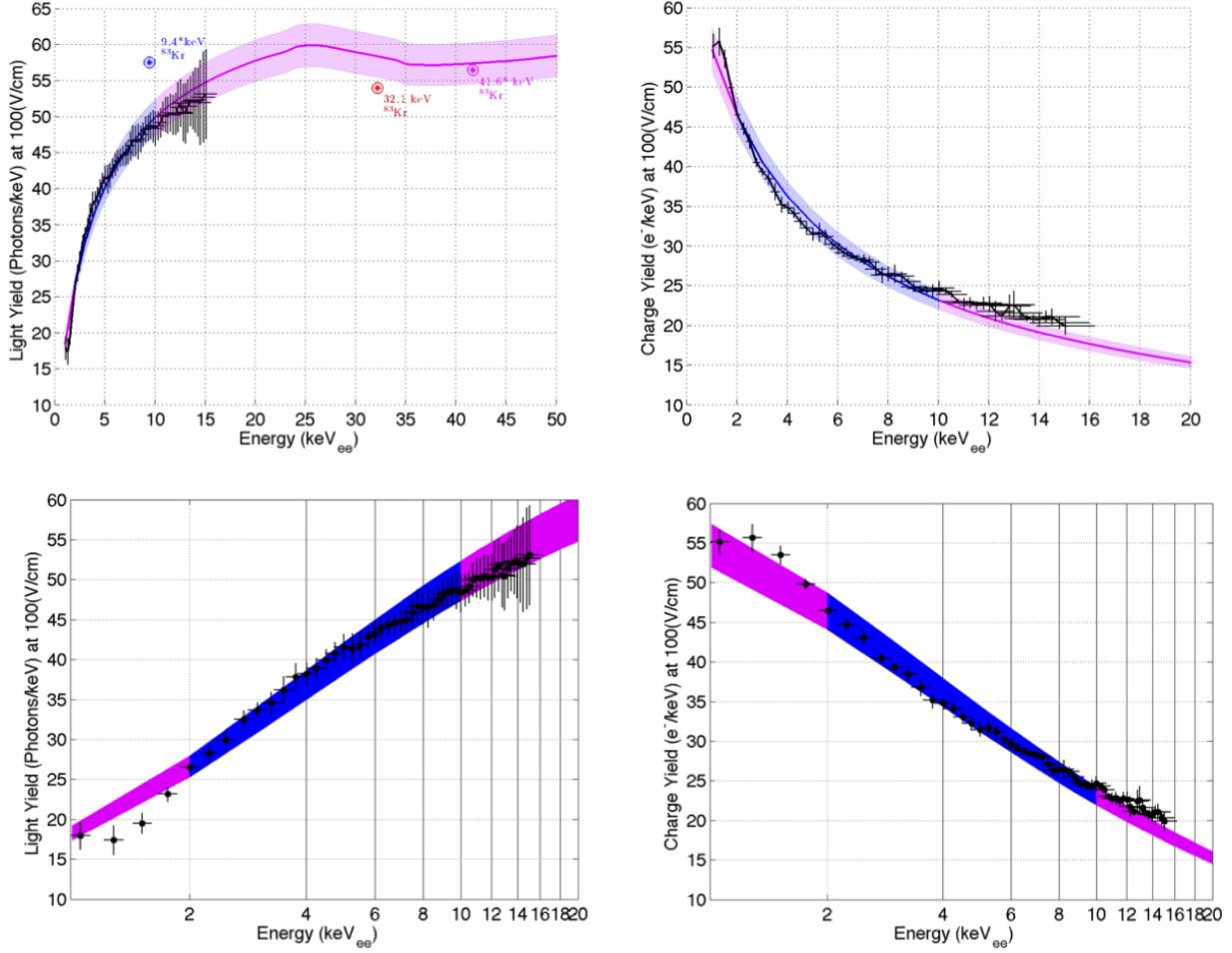


Figure 29: 105 [V/cm], corrected for spectral shape. Top Left: Mean scintillation yield vs. combined energy using tritium beta decay (black line). ⁸³Kr lines are plotted for reference but only the 32.1 [keV] line (red star) is kosher since the 9.4 [keV] line is dependent on timing separation, the 9.4 [keV] line is plotted (blue star) for separations greater than 1000 [ns]. Top Right: Mean ionization yield vs. combined energy (black line). Bottom Left: Scintillation yield vs. combined energy on a log scale. Bottom Right: Ionization yield vs. combined energy on a log scale. The shaded blue regions represent the NEST mean with $\pm 5\%$ that has been vetted by data [Erik Dahl Thesis]. The shaded magenta regions represent the NEST extrapolations from data. The measurement is made at a field of 100 [V/cm] and contains about 5,000 beta decays. The endpoint of the tritium beta spectrum is 18.6 [keV]

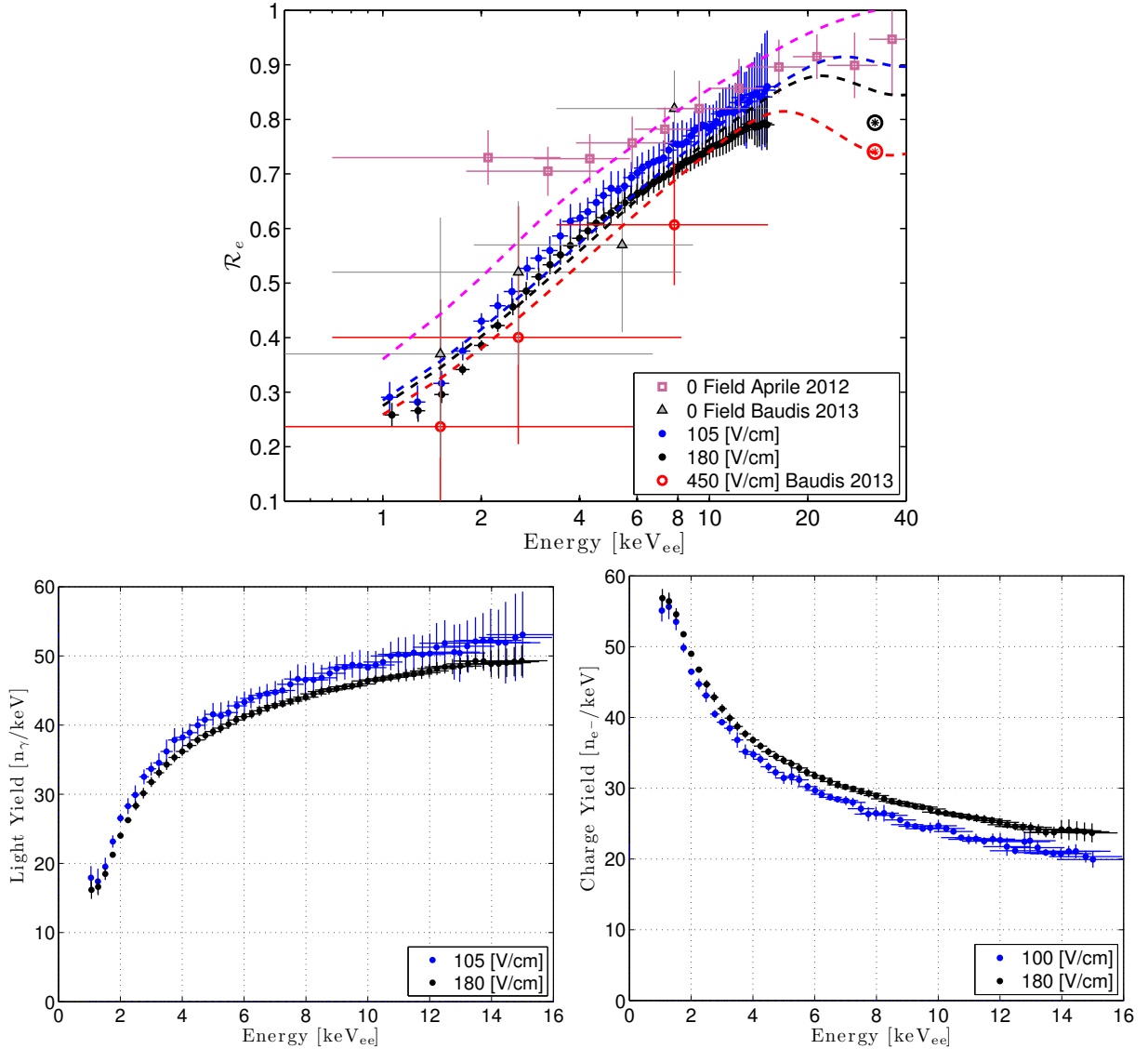


Figure 30: Top: Scintillation yield relative to the yield of the 32.1 gamma of [keV] ^{83}Kr vs. Energy. Shaded blue curve is tritium at 100 [V/cm], shaded black curve is tritium at 180 [V/cm], red points represent a recent Compton scattering measurement at 450 [V/cm]. Also shown are the corresponding quenching of the 32.1 [keV] gamma of ^{83}Kr (star inside circle). Bottom: scintillation yield [Photons/keV] vs. Energy. Shaded blue curve is tritium at 100 [V/cm], shaded black curve is tritium at 180 [V/cm], red circles represent a recent Compton scattering measurement at 450 [V/cm].

9 Discrimination vs E and S1

9.1 Discrimination vs. S1

9.2 Discrimination vs. Combined Energy

References

- [1] E. Aprile, et al. Measurement of the scintillation yield of low-energy electrons in liquid xenon. *Phys. Rev. D*, 86:112004, Dec 2012. doi:10.1103/PhysRevD.86.112004.

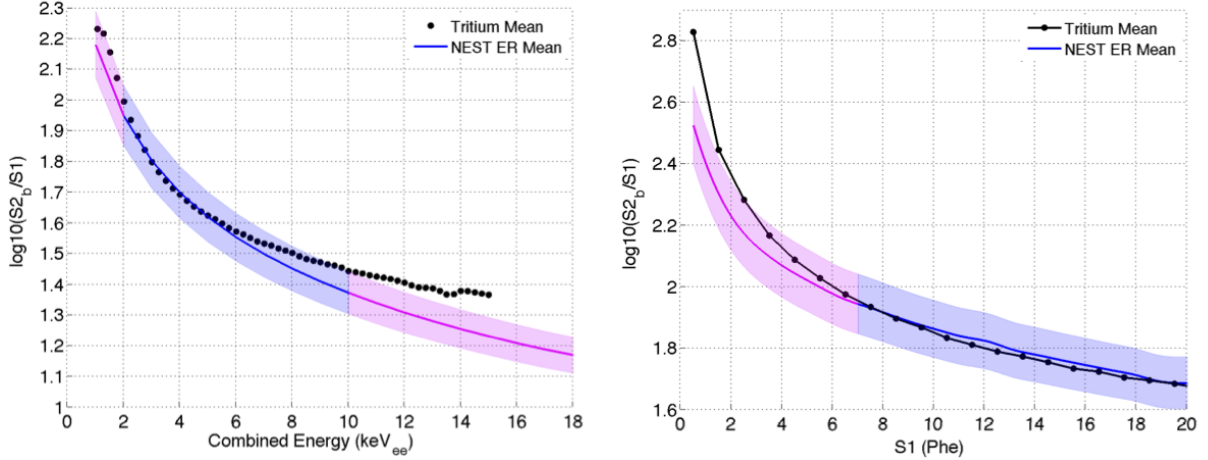


Figure 31: With S1 and S2 spectral shape correction. Left: $\log_{10}(S2_b/S1)$ (black) and NEST (shaded blue) vs. Energy. The data and the NEST prediction agree between 1[keV] to 8 [keV], where the NEST model is optimized. Right: $\log_{10}(S2_b/S1)$ (black) plotted vs S1. The shaded blue region represents the NEST mean with $\pm 5\%$. that has been vetted by data [Erik Dahl Thesis]. The shaded magenta regions represent the NEST extrapolations from data. The deviation at low S1 is potentially due to greater ionization yield than predicted by NEST at low energy.

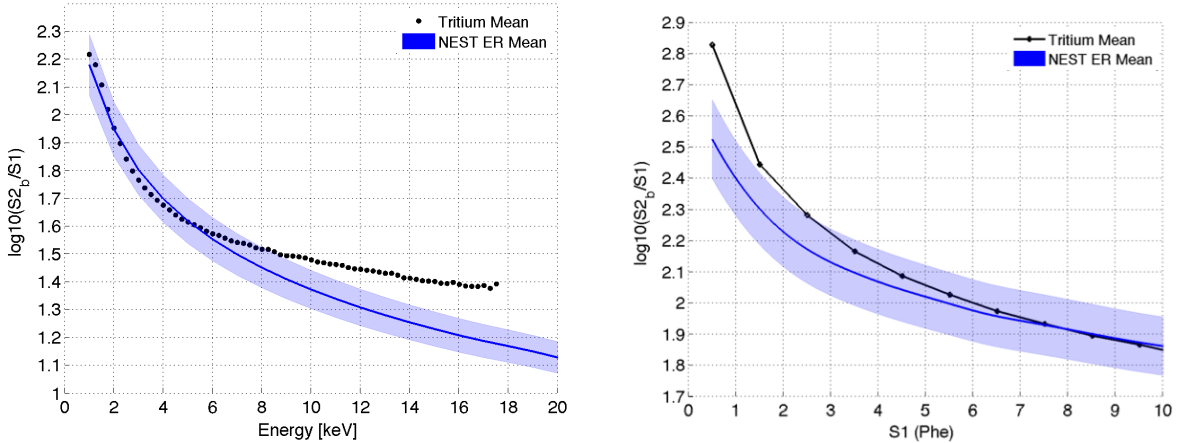


Figure 32: No spectral shape correction. Left: $\log_{10}(S2_b/S1)$ (black) and NEST (shaded blue) vs. Energy. The data and the NEST prediction agree between 1[keV] to 8 [keV], where the NEST model is optimized. Right: $\log_{10}(S2_b/S1)$ (black) plotted vs S1. The shaded blue region represents the NEST mean with $\pm 5\%$. The deviation at low S1 is potentially due to greater ionization yield than predicted by NEST at low energy.

- [2] L. Baudis, et al. Response of liquid xenon to compton electrons down to 1.5 kev. *Phys. Rev. D*, 87:115015, Jun 2013. doi:10.1103/PhysRevD.87.115015.
- [3] T. Doke, A. Hitachi, S. Kubota, A. Nakamoto, and T. Takahashi. Estimation of Fano factors in liquid argon, krypton, xenon and xenon-doped liquid argon. *Nucl. Instrum. Meth.*,

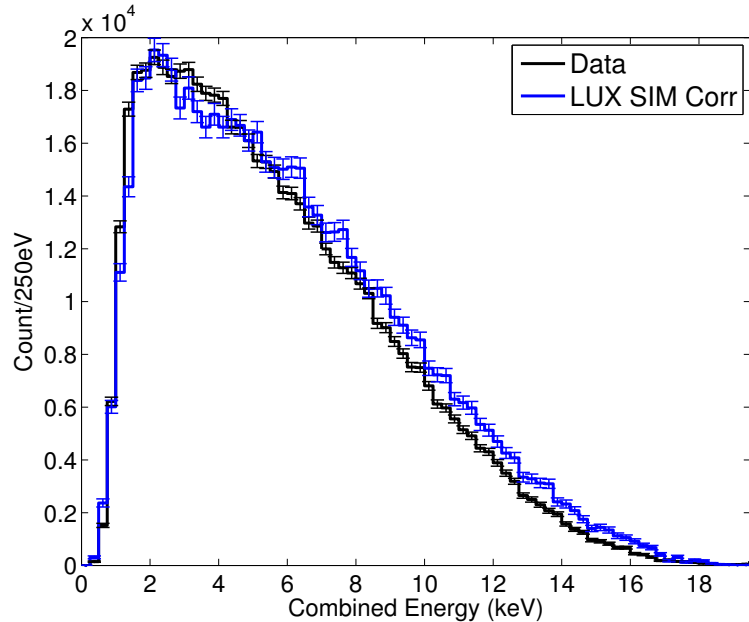


Figure 33: Tritium Data along with LUX SIM, the ‘pile up’ at low energy seen in all previous tritium energy spectra can be solved by modifying charge yield and light yield at low energies.

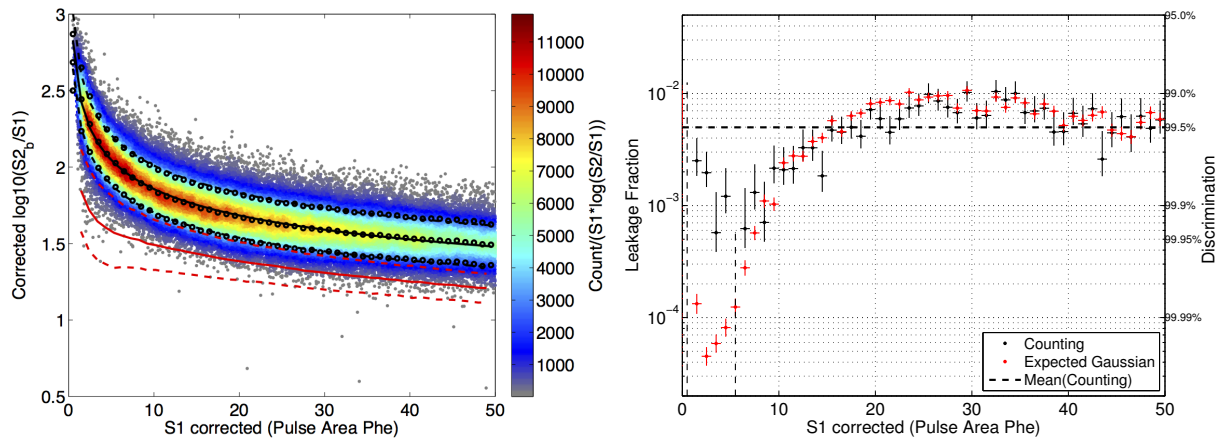


Figure 34: Discrimination vs. S1. On average from 0 to 50 Phe the discrimination is 99.50%, defined by the number of events below the mean of the nuclear recoil band. The red band represents the NEST nuclear recoil band (version 4c).

134:353–357, 1976. doi:10.1016/0029-554X(76)90292-5.

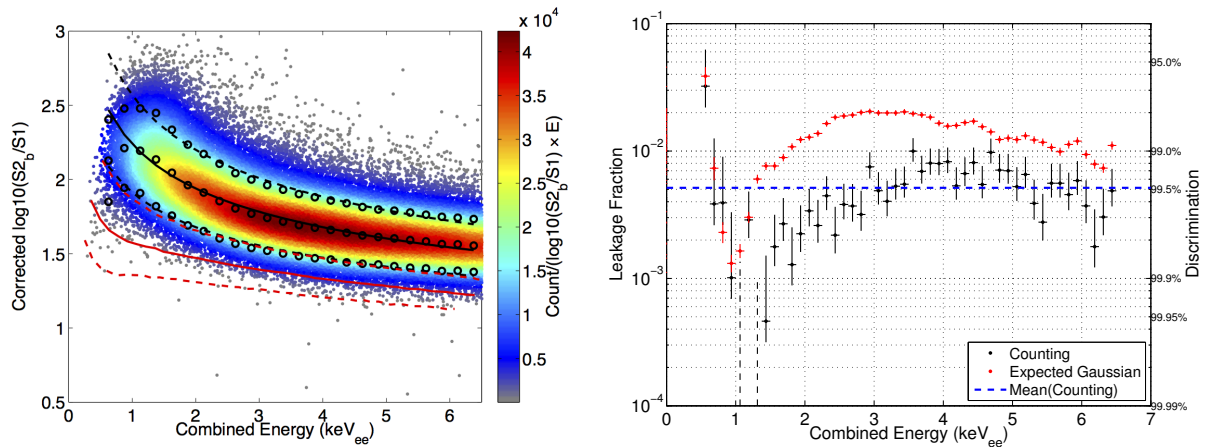


Figure 35: Discrimination vs. combined energy. On average from 0 to 6.5 keV (0-50 Phe S1) the discrimination is 99.46%, defined by the number of events of events below the mean of the nuclear recoil band. The red band represents the NEST nuclear recoil band (version 4c).